

1. Theory

The main measurement principle of a microfluidic channel in connection with a giant magneto resistance (GMR)-Sensor has been already described and characterized exhaustively by Helou [1], Reisbeck [2] and others.[3, 4] Therefore, this theoretical part will focus on (bio-)physical aspects of a cell rolling motion inside a microfluidic channel and surface modification chemistry.

1.1. Microfluidics

1.1.1. Incompressibility of Fluid Flows

The main experiments of this work were carried out in microfluidic environments, which exhibit favorable properties compared to common macrofluidic systems. From a fluid-mechanical perspective, shrinking the scales makes interfacial as well as electrokinetic phenomena much more significant, and reduces the importance of pressure and gravity.[5] However, electrodynamics, chemistry and fluid dynamics are inextricably intertwined, so that fluid flow can create electric fields (and vice versa), with a degree of coupling driven by the surface chemistry. Many of the resulting phenomena arise or can be explained by the conservation of mass described by the continuity equation (Eq. 1.1), the conservation of momentum described by the Cauchy-Momentum equation (Eq. 1.4), and the resulting Navier-Stokes equation (Eq. 1.8).

$$\frac{\partial}{\partial t} \iiint \rho \, dV = - \iint \rho \mathbf{u} \cdot \vec{n} \, dA \quad 1.1$$

$$\nabla \cdot \mathbf{u} = 0 \quad 1.2$$

$$\frac{\partial}{\partial t} \iiint \rho \mathbf{u} \, dV = - \iint \rho \mathbf{u} \mathbf{u} \cdot \vec{n} \, dA + \iint \boldsymbol{\tau} \cdot \vec{n} \, dA + \iiint \sum_i \mathbf{f}_i \, dV \quad 1.3$$

$$\rho \frac{\partial \mathbf{u}}{\partial t} + \rho \mathbf{u} \cdot \nabla \mathbf{u} = \nabla \cdot \boldsymbol{\tau} + \sum_i \mathbf{f}_i \quad 1.4$$

$$1.5$$

The foremost assumption in fluid dynamics is termed “incompressibility”, when density gradients are negligibly small to assume a uniformity thereof. This leads to a significant simplification of the conservation equations, because any transfer from kinetic to internal energy can be ignored.¹ This equation states that the mass of a control volume (in this case the volume integral over the density (ρ))) can only change by the mass flux over its unit outward normal (\vec{n}) transported by the flow field (\mathbf{u}). For constant ρ the mass does

¹ For sake of completeness, it should be mentioned that viscous forces can also transfer energy irreversibly to internal energy. However, they are inversely proportional to the system's size, and hence omitted.

never change over time. This finding and the application of Gauss's theorem yields the conservation of mass in an incompressible fluid. (Eq. 1.2)

1.1.2. Flow and Shear in Microchannels with Viscous Fluids

The final equation and Gauss's theorem can now be applied to the conservation of momentum relation. (Eq. 1.3) Integration yields then the Cauchy momentum equation which states that any change in momentum inside a control volume ($\rho \frac{\partial \mathbf{u}}{\partial t}$) is caused by convective transport for or to the volume ($\rho \mathbf{u} \cdot \nabla \mathbf{u}$), surface stresses ($\nabla \cdot \boldsymbol{\tau}$), and the volumetric net body forces (\mathbf{f}_i) such as gravity or electrostatics.

Hereby, the surface stress surface stress tensor ($\boldsymbol{\tau}$) can be further decomposed into the pressure stress tensor ($\boldsymbol{\tau}_{pressure}$) and viscous stress tensor ($\boldsymbol{\tau}_{viscous}$) as shown in the equations Eq. 1.6. Characteristically, the pressure related contributions act normal and independently from \mathbf{u} whereas viscous forces act normal and tangential, and are dependent on \mathbf{u} . The $\boldsymbol{\tau}_{pressure}$ can therefore be expressed by a scalar pressure acting in every spatial dimension which is spanned by the identity.

The viscous stresses however can not be described by a continuum equation but only by a constitutive relation of atomistic processes. The underlying fundamental model of Newton's mechanics assumes that dynamic viscosity (η) is neither dependent on any velocity nor on the strain rate. Therefor, fluids which satisfy this condition are called "Newtonian fluids". Omitting special cases such as shear-thinning, -thickening or complex colloidal fluids such as undilute blood, η is the scalar proportionality that relates the strain rate to surface stress.[5] This is captured in the equation $\boldsymbol{\tau}_{viscous} = 2\eta\boldsymbol{\epsilon}$. Thereby, the shear stress tensor ($\boldsymbol{\epsilon}$) is part of the decomposition of an unidirectional flow field. It resembles on the one hand side any stretching or squeezing of fluid by *extensional strain* and on the other hand side *shear strain* which is responsible for skewing.[5]

$$\boldsymbol{\tau} = \boldsymbol{\tau}_{viscous} + \boldsymbol{\tau}_{pressure} = 2\eta\boldsymbol{\epsilon} - p\mathbf{I}_{3 \times 3} \quad 1.6$$

$$\nabla \cdot \boldsymbol{\tau}_{viscous} = \nabla \cdot 2\eta\boldsymbol{\epsilon} = \nabla \cdot \eta \nabla \mathbf{u} \stackrel{\text{only if } \eta \text{ uniform}}{=} \eta \nabla^2 \mathbf{u} \quad 1.7$$

$$\underbrace{\rho \frac{\partial \mathbf{u}}{\partial t}}_{\text{Transient}} + \underbrace{\rho \mathbf{u} \cdot \nabla \mathbf{u}}_{\text{Convection}} + \underbrace{-\nabla p}_{\text{Pressure}} + \underbrace{\eta \nabla^2 \mathbf{u}}_{\text{Viscous}} + \underbrace{\sum_i \mathbf{f}_i}_{\text{Body Forces}} \quad 1.8$$

The divergence of $\boldsymbol{\tau}_{viscous}$, as used in the incompressible Cauchy momentum equation (Eq. 1.4), can then be simplified with Eq. 1.7 further by taking advantage of the anti-transpose symmetry of the flow field. If η is also uniform respectively isotropic across the channel, the divergence is completely independent of the scalar viscosity. Applying all assumptions to the Cauchy momentum equation (Eq. 1.4) yields as final result the Navier-Stokes-Equation (NSE). (Eq. 1.8)

However, the NSE has no analytic solution yet and can in consequence only solve defined boundary problems. The two most common boundary conditions herefore are the “no-penetration condition” ($\mathbf{u} \cdot \vec{n} = 0$) and the “no-slip condition” ($\mathbf{u}_t = \mathbf{u} - (\mathbf{u} \cdot \vec{n}) \vec{n} = 0$), which state that the normal and tangential components of fluid velocity are per definition zero at motionless, impermeable walls.

Besides these conditions, many problems arise due to turbulent flow and therefor transient effects. Mathematically, this can be avoided by simply neglecting the time-dependent term in the NSE. Also, it can be argued from a systematic point of view that, for viscosity-dominated flows, fluid moves in isoplanar “lamina”. In experimental observations, these laminar flows then proved to be steady to perturbations.

$$Re = \frac{\text{fluid density} \cdot \text{velocity} \cdot \text{size}}{\text{viscosity}} \quad 1.9$$

In a first order approximation, the dimensionless Reynolds number (Re), which compares the inertia to viscous forces, allows a qualitative prognosis about the flow regime. (Eq. 1.9) If it results below a threshold of 2300, laminar flow can be assumed in Hagen-Poiseuille flows. This holds true for the utilized microfluidic with the dimensions $15\,800\,\mu\text{m} \times 700\,\mu\text{m} \times 150\,\mu\text{m}$ ($l \times w \times h$) and aqueous buffer solutions, where the channel width considered as *characteristic size*. Hence, several fluidic phenomena such as deterministic pathlines as well as simplifications of the NSE can be exploited in the present system.

In the model case of a flow through a rectangular channel, no analytical solution of the NSE exists, but a Fourier Series expansion if the width is larger than height of a channel as shown in Bruus [6]. Equation Eq. 1.10 determines the magnitude of the flow field parallel to the pressure gradient in relation to the horizontal dimension y and vertical dimension z with respect to the channel dimensions height h and width w . An integration over the flow field in the channel cross section yields the flow rate (Q). (Eq. 1.11)²

$$\mathbf{u}_x(y, z) = \frac{4h^2 \Delta p}{\pi^3 \eta l} \sum_{n, \text{odd}}^{\infty} \frac{1}{n^3} \left(1 - \frac{\cosh(n\pi \frac{y}{h})}{\cosh(n\pi \frac{w}{2h})} \right) \sin(n\pi \frac{z}{h}) \quad 1.10$$

$$Q = \int_{-\frac{1}{2}w}^{\frac{1}{2}w} \int_0^h u_x(y, z) \, dz \, dy \approx \frac{h^3 w \Delta p}{12 \eta l} \left(1 - \frac{h}{w} \right), \text{ for } h < w \quad 1.11$$

² The equation Eq. 1.10 shows that height deviations can have prominent influence on a channel velocity simulation as it is proportional to h^2 . Further, the flow rate depends even on h^3 .

1.1.3. Force Equilibrium of Microbeads

Although microfluidic systems mostly operate in a low inertia regimes as specified by low Re , the force equilibrium $\sum_i \mathbf{F} = 0$ and subsequently the velocity of any particle in the fluid stream is influenced as it moves closer to the boundaries. Several models have already been implemented with a part of the mentioned forces. Lee and Balachandar [7] compared the importance of translation, rotation and shear forces. Dong and Lei [8] evaluated cell rolling characteristics, and Wu and Voldman [9] proposed a model for bead-based immunoassays in microfluidics. Therefore, an overview over all (inter-)acting forces shall be given here.

$$Re_{particle} = \frac{r^2}{\frac{2wh}{w+h}} Re \quad 1.12$$

Additionally to the channel Reynolds number Re , describing the ratio between inertial force and viscous force of fluid in a flow, Di Carlo et al. [10] proposed a particle Reynolds number ($Re_{particle}$) considering the size ratio of particle to channel. At $Re_{particle} \ll 1$, particles are subjected to the dominant viscous drag to follow fluid streamlines. In the contradictory case, inertia becomes prominent. However, on increasing $Re_{particle}$ to the order of 1, inertial lift forces become dominant and lateral migration of particles across streamlines becomes visible. For a micrometer sized bead and a channel as referred to in Sec. 1.1.2, the pre-factor is in the range of 1×10^{-5} to 1×10^{-7} hence viscous drag overweighs inertial lift of a particle.

Stoke's Drag

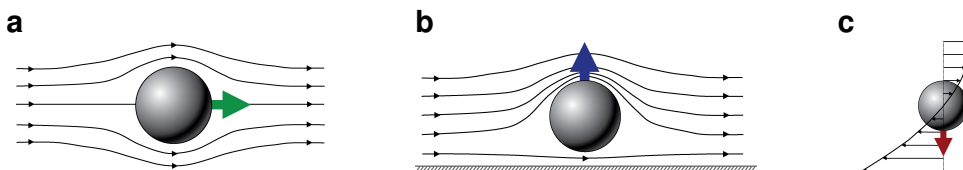


Figure 1: Particle Drag and Lift Behavior

(a) Bulk Drag: Force acts on a particle caused by the displacement of fluid stream lines. (b) Wall-lift Drag Force: In a special case of drag, where streamlines cannot be displaced further, a pressure gradient forms in front of the sphere. This forces a motion directed perpendicularly from the wall. (c) Shear-induced force: The curvature of the flow profile exhibits a translation and rotation due to inhomogeneously distributed shear on the surface.[11]

The foremost force to actuate particles inside a microfluidic channel is Stoke's drag force (\mathbf{F}_{drag}). (Eq. 1.13) It originates from viscous fluid moving past the sphere surface, where a slip condition has to be applied. The fluid therefor has to displace its elements in front of the movement direction.[12] A particle with the surrounding streamlines is depicted

in Fig. 1a for the bulk case and in Fig. 1c for adjacent walls.

$$\mathbf{F}_{drag,wall} = -6\pi\eta r \bar{\mathbf{u}} K \quad 1.13$$

$$K = \frac{4}{3} \sinh \alpha \sum_{n=0}^{\infty} \left(\frac{n(n+1)}{(2n-1)(2n+3)} \cdot A \right) \quad 1.14$$

$$\alpha = \cosh^{-1} \frac{z}{r}, \quad 1.15$$

$$A = \frac{2 \sinh((2n+1)\alpha) + (2n+1) \sinh 2\alpha}{(2 \sinh((n+0.5)\alpha))^2 - ((2n+1) \sinh \alpha)^2} - 1 \quad 1.16$$

$$K_{approx} = \frac{24}{Re} * \left(\frac{1 + \frac{2}{3}\lambda}{1 + \lambda} \right), \text{ with } \lambda = \frac{\eta_{fluid}}{\eta_{particle}} \quad 1.17$$

$$v_z = \frac{3}{64} Re_s \mathbf{u}_s = \frac{3}{64} \frac{\rho_{fluid} r \mathbf{u}_s}{\eta} \mathbf{u}_s, \left(\frac{\rho_{fluid} l_w \mathbf{u}_s}{\eta} \right) \ll 1 \quad 1.18$$

$$\omega = \frac{3\mathbf{u}}{32r} \left(\frac{r}{l} \right)^4 \left(1 - \frac{3}{8} \frac{r}{l} \right), \text{ for } \left(\frac{r}{l} \right)^2 \ll 1 \quad 1.19$$

In the proximity of a channel wall, where no fluid can be displaced further, a correction factor was determined by Happel and Brenner [13] that approximates drag in a perpendicular direction.(Eq. 1.14) Repulsion velocity can then be defined by the Reynolds number calculated with a sedimentation velocity (\mathbf{u}_s) if the particle center has a distance $l_w \ll 1$ from the wall.[14, 15] A phenomenological approximation of the correction factor yields equation Eq. 1.17, when viscosity dominates the difference. Adapted to an example, a spherical air-bubble inside a water flow feels only 67.4 % of the drag by surrounding fluid.

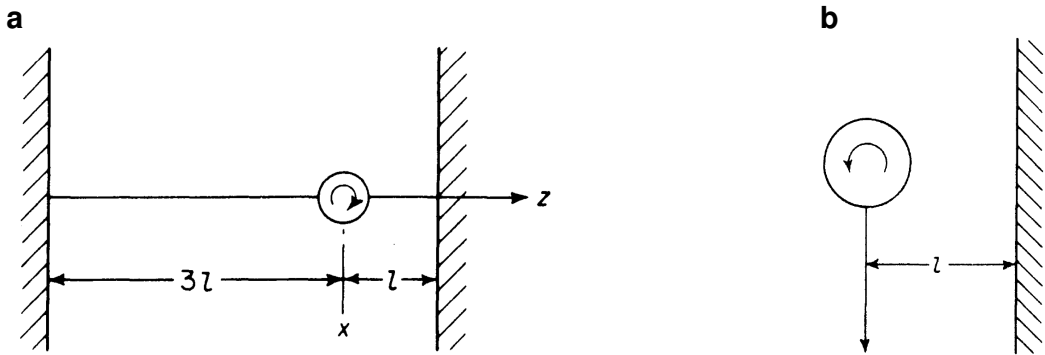


Figure 2: Particle Rotation Behavior

(a) Direction of rotation of a sphere settling in eccentric position between parallel walls. (b) Direction of rotation of a sphere settling in the presence of a single plane wall far from the other side.[10]

The considerations of Stoke's drag force above were limited for only linear translation cases. However, fluid drag also imposes a non-negligibly torque on particles if a particle moves nearer than 10 diameters to the wall. Happel and Brenner [13] mention an experimentally determined formula in 1.19 to calculate a drag-related angular rotation frequency (ω). Counter-intuitively, the direction of rotation in the bulk fluid (Fig. 2a) is opposite than from the rotation direction near or touching the wall (Fig. 2c). This can be explained by a complex superposition of tangential components from later mentioned forces and will not be explained to any more extent here.

Gravity and Buoyancy

On every mass in our environment acts gravity (\mathbf{F}_{grav}) to pull it along its gradient. In a medium, notwithstanding, it is balanced by the displacement of the same in the counter-direction called buoyancy ($\mathbf{F}_{buoyancy}$). As a microparticle made from a co-polymer - especially when it carries magnetic momentum - has a significantly higher density than water, \mathbf{F}_{grav} (Eq. 1.21) outperforms $\mathbf{F}_{buoyancy}$ (Eq. 1.20), which in term causes a particle to sink to the channel floor.

$$\mathbf{F}_{buoyancy} = -\frac{4}{3}\pi r^3 \rho_{fluid} g \quad 1.20$$

$$\mathbf{F}_{gravity} = +\frac{4}{3}\pi r^3 \rho_{particle} g \quad 1.21$$

Magnetic Force

The - during the course of this thesis - strongest acting force is exhibited by the magnetic flux density (\mathbf{B}), which acts on paramagnetic particles with a magnetic dipole moment (\mathbf{m}). When an external magnetic field is non-uniform, there will be a magnetic force (\mathbf{F}_{mag}), proportional to the magnetic field gradient, acting on the magnetic dipole moment.(Eq. 1.24) For particles that carry magnetite or similar ferrimagnetic material in their polymer shell, the magnetic momentum can be inferred by the relation $\mathbf{m} = \mathbf{M}V$ if the magnetization (\mathbf{M}) of a volume V is known. However, the more exact approach is a comparison of magnetic susceptibilities (χ) as described in Eq. 1.22. Consequently, if the particle susceptibility is greater than the fluid's, a microbead will move towards the field maximum. Calculated for an $8\text{ }\mu\text{m}$ bead with $1.12 \times 10^{-12}\text{ A m}^2$ saturation magnetization, \mathbf{F}_{mag} results in $\sim 45\text{ pN}$ for a field gradient of 5 T m^{-1} .

$$\mathbf{F}_{mag} = \frac{V_p(\chi_p - \chi_f)}{\mu_0} (\mathbf{B} \cdot \nabla) \mathbf{B} \quad 1.22$$

$$\mathbf{F}_{dipole} = (\mathbf{m} \cdot \nabla) \mathbf{B} = -\nabla \mathbf{E}_{dipole} \quad 1.23$$

$$\mathbf{E}_{dipole} = \sum_{i=1}^n \frac{\mu_0}{4\pi r_i^3} \left(\mathbf{m}_i \cdot \mathbf{m}_{ref} - \frac{3}{|\mathbf{r}_i|^2} (\mathbf{r}_i \cdot \mathbf{m}_i)(\mathbf{r}_i \cdot \mathbf{m}_{ref}) \right) \quad 1.24$$

Additionally, the magnetic beads interact with each other according to the dipolar interaction. In that case, a reference bead with magnetic momentum \mathbf{m}_{ref} at distance \mathbf{r}_{ref} feels the force of all surrounding particles. (Eq. 1.24)

Electrostatic Interaction

The microchannel - as well as a particle in it - carries an electrical double layer on the surface due to present surface charges. The net charge acquired by the particles can be computed by integrating the particles' surface charge densities over their surfaces as described by Gauss's Law. However, as Coulomb's force (\mathbf{F}_{el}) on charge q_1 is square dependent of the distance from the secondary charge q_2 at the respective locations $\mathbf{r}_1, \mathbf{r}_2$.(Eq. 1.25) This, and the fact that the surface net charge in a buffer solution is insignificant, lead to the assumption that \mathbf{F}_{el} plays a minor role in this force equilibrium.

$$\mathbf{F}_{el} = \frac{q_1 q_2}{4\pi\epsilon_0} \frac{\mathbf{r}_1 - \mathbf{r}_2}{|\mathbf{r}_1 - \mathbf{r}_2|^3} \quad 1.25$$

Magnus Lift Force

The Magnus lift force (\mathbf{F}_{magnus}) is a rotation-induced variable as a result of the pressure difference induced by streamline asymmetry.[16] For a spinning particle in a fluid

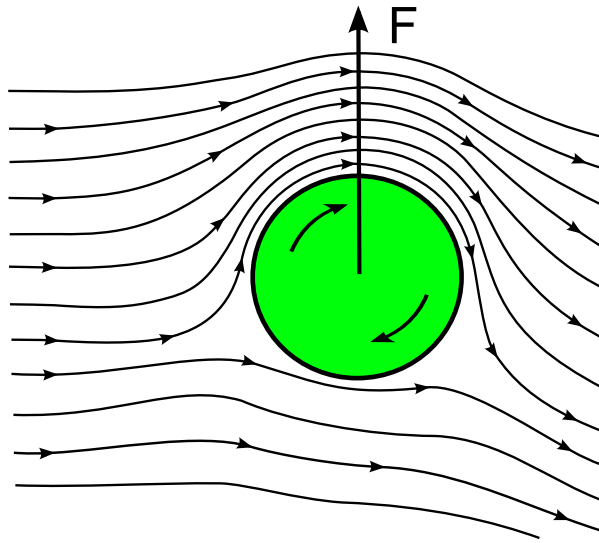


Figure 3: Magnus Effect on a Particle in Laminar Flow

The intrinsic rotation of a particle inside a laminar flow field causes a pressure gradient to the side whose tangential rotation vector is parallel to the stream lines.

as shown in Fig. 3, the streamline density and therefore the pressure on the one side of the particle is lower relative to the other side. The main driver of this effect is again the no-slip boundary, where fluid on the front side of the particle is dragged down whereas the fluid on the bottom side is slowed down. As a result, this leads to a lift force perpendicular to the flow direction.

$$\mathbf{F}_{magnus} = \frac{1}{8} \pi r^3 \rho_{fluid} (\mathbf{u} \times \boldsymbol{\Omega}) \quad 1.26$$

Saffman Lift Force

When the rotation speed of a particle in shear rate direction is much greater, $\boldsymbol{\Omega} > 12\nabla\mathbf{u}$, for a freely rotating particle Saffman lift force ($\mathbf{F}_{saffman}$) will begin to act. Depending on the interaction of slip velocity and shear, it will counteract any movement to the planar surface. Hence, at high gradients the center of rotation causes a shift to the maximum shear.

Scaling with ω , it will generally be at least one order of magnitude larger than Magnus force. Especially for electrically or magnetically actuated particles, shear-induced lift force (\mathbf{F}_{shear}) is more relevant in the case of non-neutrally buoyant spheres.[16]

$$\mathbf{F}_{saffman} = \frac{81.2}{4} (\mathbf{u} - \mathbf{u}_p) r^2 \sqrt{\frac{\rho_{fluid}}{\eta}} \nabla \mathbf{u} \quad 1.27$$

Shear-induced Lift Force

This \mathbf{F}_{shear} particles to migrate toward walls until the wall lift force repels and balances it. In contrast, if the curvature of \mathbf{u} is zero, it collapses to a simple shear flow. Then the pressure will be higher on the far from the center pushing particles to the centerline of channel. As shown in Fig. 1e the magnitude of \mathbf{u} in particle is much higher on the top side of particle than that on the bottom side, due to the parabolic nature of velocity profile. Similar to Saffman force, the dissymmetry of relative velocity causes a lower pressure on the wall side, generating a shear gradient lift force which is opposite to the Saffman force.[16]

$$\mathbf{F}_{shear} = K \rho_{fluid} (\nabla \mathbf{u})^2 r^4, \text{ with } K \text{ from Eq. 1.17} \quad 1.28$$

Deformability-Induced Lift Force

Although solidity can assumed in the first order to the study of hydrodynamic behaviour of particles in a microchannel, cells and vesicles are not rigid but deformable. The deformability will induce an additional lift forces on the particles, which is perpendicular to the main streamline, and it is subjected nonlinearities caused by the matching of velocities and stresses at the deformable particle interface.

$$\mathbf{F}_{deformation} = \mu U r \left(\frac{r}{H} \right)^2 \frac{l_w}{H} f(\lambda) \quad 1.29$$

$$f(\lambda) = \frac{16\pi}{(\lambda+1)^3} \left[\frac{11\lambda+10}{140} (3\lambda^3 - \lambda + 8) + \frac{3}{14} \frac{19\lambda+16}{3\lambda+2} (2\lambda^2 - \lambda - 1) \right] \quad 1.30$$

For example, deformability-induced lift force has been used already to separate and enrich malaria-infected red blood cell (RBC) from normal healthy RBC for the diagnosis of malaria. The parasite releases proteins that trigger the cross-linking of the spectrin network of the membrane, thus increases the rigidity of the infected cells.[17] Mach and Di Carlo [18] reported a parallelized microfluidic device that passively separates pathogenic bacteria from the diluted blood by the use a unique differential transit time due to channel height differences which in turn caused size-dependent inertial lift forces to obtain cell separation.

Fåræus and Fåræus-Lindquist Effect

Often confused, the Fåræus and Fåræus-Lindquist effect constitute two different hemodynamic properties relevant for microfluidics with blood samples. Whereas the Fåræus effect states that RBCs are depleted in the wall regions of capillaries (due to the lift forces mentioned before), the Fåræus-Lindqvist effect describes the behavior of blood

to decrease its viscosity in narrow channels.[19, 20] Thereby, the latter effect is not solely driven by the first, but also the Segré-Silberberg effect, who discovered that for neutrally buoyant particles an equilibrium at exact $0.6r$ from a tubing center forms.[21] To model this effect, Chebbi [22] developed a cell-free marginal layer model.

1.1.4. Rolling Motion and Surface Interaction of Beads

A nice intro goes here

Contact Area of a Sphere and Flat Surface

Once the acting forces brought the bead in contact with a wall or the channel bottom, it starts to move forward in a rolling motion. In a simple model, rolling on a plane without slipping is constrained by a sphere's translation (\mathbf{F}_{\parallel} , \mathbf{F}_{\perp}), rotation (ω), and shear. Nevertheless, due to the rigid nature of the sphere, any shear will be omitted in further models.[23] The no-slip boundary condition has to be applied also here by the requirement that the points of the sphere momentarily in contact with the plane are at rest. However, rolling contact problems are dynamic because the contacting bodies are continuously moving with respect to each other. The contact patch in a sliding problem continuously consists of the same particles. In contrast, particles enter and leave the contact area during rolling. Moreover, in a sliding problem the surface particles in the contact patch are all subjected the same tangential shift everywhere, whereas in a rolling problem the surface particles are stressed in different ways. During rolling, they are free of stress when entering the contact, then stick to a particle of the opposing surface, and are strained by the overall motion difference between the two bodies, until the local traction bound is exceeded and local slip sets in.[24]

In a real world, pressing two bodies with rough surfaces against each other limits the contact between the two bodies to a value, which is much smaller than the nominal contact area. Additionally, on natural and engineering surfaces Lennard-Jones potential, wetting, and molecular interactions start to play a role on the spectated microscale.[25]

In reality, with elastic effects taken into consideration, a different situation occurs. If an elastic sphere is pressed onto an elastic plane (ideally of the same material), both bodies deform and a Hertzian pressure distribution arises. The center of the sphere is moved down by an approach (z) as shown in Fig. 4 that can also be described as "maximum penetration distance". It can now be calculated that the normal contact area between the bodies follows $A_{contact} = \pi a^2 = \pi (2rz - z^2) = 2\pi r z (1 - \frac{z}{2r})$. Assuming that $z \ll 2r$ and considering that $A_{contact}$ must be zero for all $z < 0$, the following equation for the contact area arises. (Eq. 1.31) The spherical contact surface can be calculated analogous Eq. 1.32.[25]

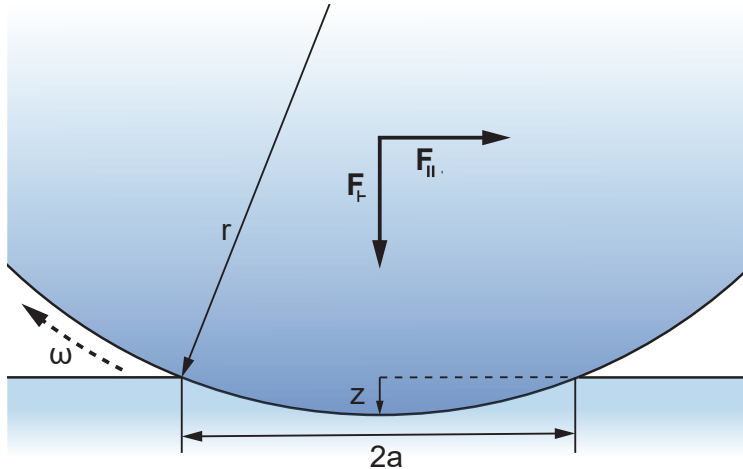


Figure 4: Rolling Mechanics of a Sphere

Penetration model of a sphere with radius r adapted from Azad and Featherstone [25] and Waters and Guduru [26]. The top body moves into the elastic bottom body for an approach (z) and a contact area πa^2 .

$$A_{contact} = 2\pi r z, \text{ for } z \geq 0 \quad 1.31$$

$$S_{contact} = \pi r(2z + a^2) = \pi z(4r - z), \text{ for } z \geq 0 \quad 1.32$$

For a $8\text{ }\mu\text{m}$ microbead and a penetration depth z of 100 nm this yields for example an interaction with 6.84% of the total sphere and a total area of $13.753\text{ }\mu\text{m}$. Several methods and experiments have already been developed in the literature to measure the resulting friction and penetration parameters. A general model of a sphere in contact with a wall was optimized by Krishnan and Leighton [27]. Experimentally, Waters and Guduru [26] developed a microtribometer in PDMS to evaluate adhesion properties and validate their model's predictions.

Protein interaction during Rolling

In the attempt to mimic rolling adhesion on vascular surfaces which is the first step in recruiting circulating leukocytes and other cells into the tissue, protein-protein-interactions as driver for microbead motions have been studied extensively in this thesis. Statistically, a cell flowing near the vessel wall is able to attach if its adhesion receptors contact ligands on the wall. Bond formation, anyhow, involves distinct steps: transport, which brings two molecules into close proximity, and reaction, during which the molecules dock. Faster cell velocity produces more collisions but also limits the interaction time between interaction molecules. Thus, the relative timescales for transport and docking affect the efficiency of tethering a flowing cell to the surface.[28]

For these properties, Dembo et al. [29] developed a detailed physical description of membrane adhesion and detachment kinetics. Wu and Voldman [9] then proposed an

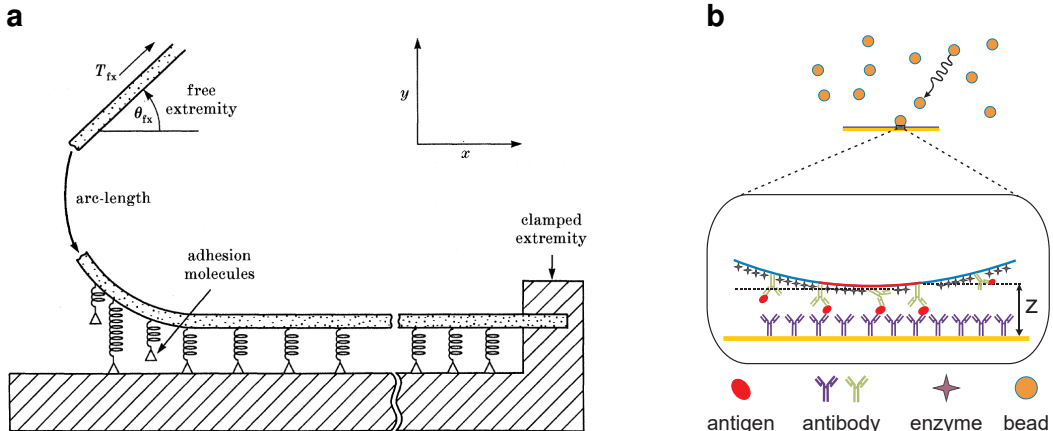


Figure 5: Membrane Adhesion and Detachment Models

a Adhesion Model after Dembo et al. [29]: Every interaction is viewed as spring-damper-model in superposition. b Surface Coverage Assay Model: In a stochastic approach, analyte molecules and their interactions are modeled between a planar and a spherical surface. Adapted from Wu and Voldman [9]

integrated model for bead based rolling mechanisms under the influence of protein interaction. The key for interaction thereby is the specific *affinity* respectively *avidity* of the protein and its ligand. In general, high-affinity ligand binding results from greater attractive ligand-receptor-forces and results in a higher tenacy of the receptor. However, lifetime of a formed complex does not correlate. The net ligand affinities are unitized by the dissociation constant (K_d), which relates the reverse reaction rate ("the dissociation of the bond") to the forward reaction rate ("the formation of the bond"). Therefor high-affinity results in low K_d .

On a bead and microchannel surface, however, not only one but multiple protein-ligand complexes are formed and dissociated simultaneously. This is described by *avidity*. Through single binding events elevate the likelihood of other interactions, avidity is not relating the sum of its ingredient affinities but can rather be seen as the combined effect of all affinities participating in the biomolecular interaction.[30]

Main factor for the method in this thesis is now the critical tension (T_{crit}). A particle - cell or bead - flowing in a low-Reynolds number environment, experiences a F_{shear} and a torque rotation vector (Ω), which both reach maximum when the particle stops. For this, the two forces must be counteracted by a tensile force on the adhesive bonds and a compressive force at the bottom of the particle. Moreover, these forces affect the forward and reverse reaction rates of the bonds. Any rolling motion stops when the adhesion can withstand the force required to counteract the maximal other forces. After break-up of this bonds the particle begins to accelerate downstream until a newly formed bond develops sufficient strength. Consequently, the intrinsic mechanics of these bonds and how their respective off-rates act under force critically determines whether and how bead roll in a flow field.[28]

There exist two distinct bond types that take effect during the above processes: *Slip*

bonds are linkages whose lifetime is shortened to some extent by external force whereas *catch bonds* lock more tightly upon deformation stress.

In biological systems, for example selectines, another effect arises. Upon increasing external stress, bond lifetimes with the ligand are first prolonged until a threshold where bonds are starting to decease. In contrast, if an antibody is the ligand only slip bonds are formed in response to force.[31, 32] By studying the exact forces acting on a particle-protein interaction system affinity based sorting and ultrasensitive assays can be established.[33]

1.2. Surface Chemistry

Introducing biological samples, such as peripheral whole blood and -plasma, into microsystems needs careful consideration of surface modification compared to buffered samples of adjusted pH containing cells or polymeric beads. Blood-material contact most often initiates surface-mediated reactions that lead to cell activation, blood clotting or biofilm formation.[34, 35] In order to minimize unspecific interactions on surfaces, most contact faces are passivated with chemically and biologically inert materials or even composed entirely from it. In any use case, where a surface has to be functionalized with biomolecules, the intrinsic inertness then requires specialized methods for permanent and reproducible adhesion.[36, 37]

Molecules can be immobilized through various mechanisms on surfaces to achieve a biological or chemical functionality. The most simple is physisorption. Here, a biomolecule is bonded only by weak electrostatic, van-der-Waals or dipole-dipole interaction with a adsorption enthalpy below 50 kJ mol^{-1} .[37] In contrast, this yields fast reaction rates, because no activation energy has to be overcome. Although a large number of molecules can be captured with this method, several drawbacks have been identified.[38–41] Therfore, most functionalization approaches rely on chemisorption where molecules are covalently bound to a surface. Due to the higher activation energy barrier this bonding mechanism works slower in comparison to physisorption, though higher temperatures or catalysts can promote an equilibrium. One of the most well-known strategies to bring reproducible thin films on surfaces is the formation of self-assembled monolayers (SAMs) where a dense layer of single molecules with high internal order forms upon dipping into a surface-active substance.[42]

1.2.1. Surface Oxidation Methods

Modifying a surface with functional silanes, requires oxidized sites, for example $-\text{OH}$ (hydroxyl) resp. $\text{Si}-\text{OH}$ (silanol) groups. In order to increase the presence of those reactive groups on substrates, various activation methods such as a mixture from hydrogen peroxide with excess of sulfuric acid (piranha) and sulfuric acid (H_2SO_4), oxygen gas (O_2) - plasma treatment or an hydrofluoric acid (HF) dip can be chosen.[43]

Critical for any surface engineering is the internal structure and in consequence the binding energies of the surficial groups. The three mainly used substrates in this work, glass, poly(dimethylsiloxane) (PDMS) and silicon nitride (Si_3N_4), contain highly conserved, homogeneous surfaces and are mostly well characterized. The surface of glass exhibits already silanol groups intrinsically and consequentially demands only a removal of impurities. PDMS and Si_3N_4 however have different compositions as shown in Fig. 6 and ?? hence requiring a strong oxidation agents to completely exchange its interface to hydroxyl.[44–46]

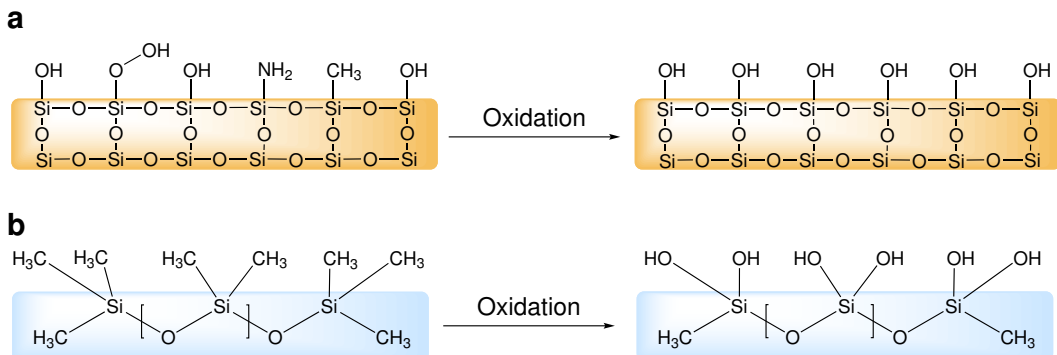
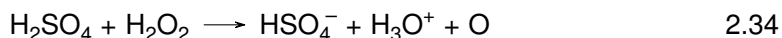
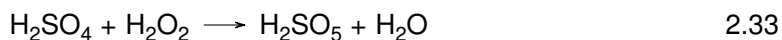


Figure 6: Different Substrate Surfaces: Glass, PDMS and Si_3N_4

Surface groups and internal structure of quartz glass (a), PDMS (b), and silicon nitride (c). After an oxidation step, the methyl groups are converted to hydroxyl.

Piranha Solution

Piranha is an oxidizer composed of hydrogen peroxide (H_2O_2) and H_2SO_4 , typically in volume ratios between 1:3 and 1:7. The effectiveness of piranha in removing organic residues and creating hydroxyl groups is induced by two distinct processes. First, hydrogen and oxygen are removed as units of water by the concentrated H_2SO_4 in a comparably fast process. (Eq. 2.33) This occurs due to the thermodynamically favorable reaction with an enthalpy of -880 kJ mol^{-1} and produces Caro's acid (H_2SO_5), one of the strongest oxidants known.[47]



Second, the sulfuric acid boosts hydrogen peroxide from a mild oxidizer into the more aggressive atomic oxygen by the dehydration of H_2O_2 . (Eq. 2.34) These two dehydration processes result on the one hand in a highly corrosive nature against organic materials, particularly against the difficult to remove carbon. On the other hand, it is strongly acidic and oxidizing.

Hydrofluoric Acid

One of the substrates used in this work is Si_3N_4 as passivation layer above magnetic sensors as it has a significant better diffusion barrier against water or sodium ions and is chemically inert.[48] However, due to its complex crystal structure it is also difficult to modify by common chemicals and the exact surface composition still subject to scientific discussion.[49] Apart from cleaning the surface with piranha, few other modification methods have been reported, but only one suitable for the direct generation of hydroxyl groups.[42, 49–51]

As depicted in Fig. 6, the reaction $\text{Si}-\text{OH} + \text{HF} \leftrightarrow \text{Si}-\text{F} + \text{H}_2\text{O}$ takes place reversibly due to the coincidence that $\text{Si}-\text{O}$ and $\text{O}-\text{H}$ as well as $\text{Si}-\text{F}$ and $\text{H}-\text{F}$ bonds have similar binding energies. Hence, the forward and reverse reactions require a low activation energy. After Le Chatelier's principle, a depletion of HF in the bulk leads then to an increase in surficial hydroxyl groups.[52] It was revealed that an oxidation with a similar protocol based on aqueous HF yields a variable $\text{Si}-\text{O}-\text{Si}$ (siloxane) coverage with $37 \pm 17\%$ of a monolayer, which can be used for stable, covalent attachment of silanes. Nominally, the same surface coverages of silicon oxide and nitride surfaces could be achieved by ethoxy- and chlorosilanization.[53] As shown by Gustavsson et al. [54], the subsequent surfaces exhibit beneficial biological properties and can be modified by further standard procedures.

Oxygen Plasma

Apart from wet chemistry methods, the exposure of a surface to oxygen plasma yields hydroxyl groups as well. In a plasma chamber, a low-pressure gas is irradiated by kHz to MHz waves to excite and ionize its atoms. In consequence, the UV-radiation emitted by the gas can photolyse typical organic bonds and remove surface contaminations. Additionally, reactive oxygen species such as O_2^+ , O_2^- , O_3 or O oxidize the surface or bind dissociated components with low vapor pressure. During an evacuation in the process, these molecules are removed from the chamber intrinsically.[55]

1.2.2. Silane Chemistry

By the use of silane chemistry a surface is rendered organofunctional with alkoxysilane molecules. Since glass, silicon, alumina, titania, and quartz surfaces, as well as other metal oxide interfaces, are rich in hydroxyl groups, silanes are particularly useful for modifying these materials.[56]

The general formula for a silane coupling agent (Fig. 7a) typically shows the two classes of functionality. X is a hydrolyzable group typically alkoxy, acyloxy, halogen or amine. Following hydrolysis, a reactive silanol group is formed, which can condense with other silanol groups to form siloxane linkages. (Fig. 7) Stable condensation products are also formed with other oxides such as those of aluminum, zirconium, tin, titanium, and nickel. Less stable bonds are formed with oxides of boron, iron, and carbon, whereas alkali metal oxides and carbonates do not form stable bonds with siloxanes at all. The R group (Fig. 7a) is a nonhydrolyzable organic radical that may possess a functionality that imparts desired characteristics. One of the more common silanes is 3-triethoxysilyl-propan-1-amine (APTES), where the X group consists of an $-\text{O}-\text{CH}_2-\text{CH}_3$ (ethoxy) group, the organic rest R is substituted by an $-\text{NH}_2$ (amine) and the 3 $-\text{CH}_2-$ (methylene) groups alter n to 3.[57]

The final result of reacting an organosilane with a substrate ranges from altering the adhesion characteristics, catalyzing chemical transformation at the heterogeneous in-

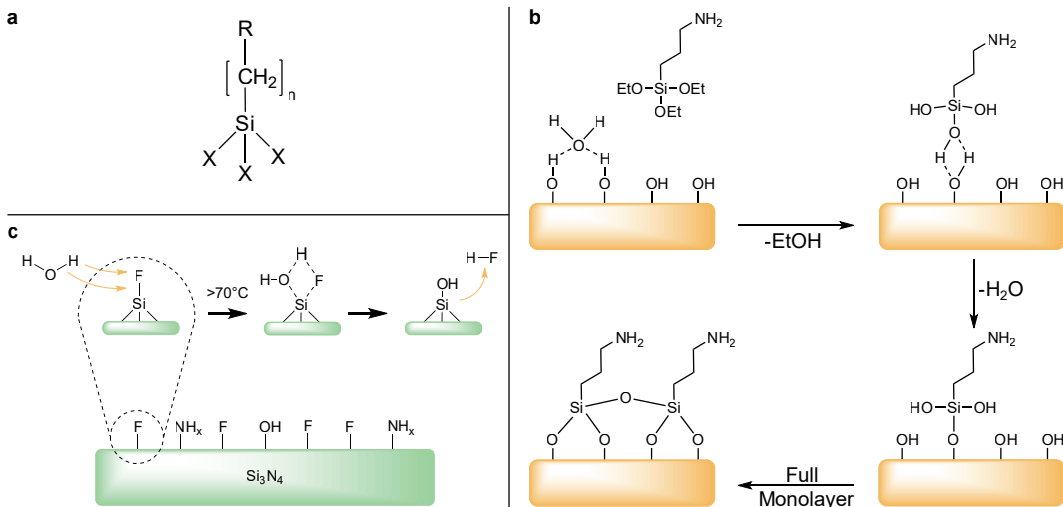


Figure 7: Surface Oxidation and Modification by APTES

(a) Structure of a typical trialkoxysilane, X: hydrolyzable group, R: non-hydrolyzable organic radical, n: methylene chain-length. (b) Before the condensation reaction, the oxidized surface has formed hydrogen bonds with water molecules while the silane molecules are in the bulk solution. The hydrolyzed silanol group adsorbs onto the surface and forms hydrogen bridges with the silicon bound oxygen atom. In a condensation reaction, under the loss of water, a covalent bond to the surface forms. After the SAM assembly the surface is saturated with a covalent-bound, crosslinked silane film.[58] (c) Proposed oxidation of Si_3N_4 with HF: Due to similar activation energies water can displace HF in a competitive manner effectively above a temperature above 70 °C.

terface, ordering the interfacial region, and modifying its partition characteristics. Significantly, it includes the ability to effect a covalent bond between organic and inorganic materials. Especially in optical or biological sensors, silane modifications open a broad range of applications.[42, 59, 60]

However, the silanization reactions bear a few drawbacks which are often neglected. For instance, silane chemistry is strongly temperature and pH-dependent.[61, 62] Further, in a process to build SAMs from APTES, the reaction must be catalyzed by water. But already small changes in the water content cause dramatic deviations in layer thickness.[63] Additionally, silanes can crosslink to themselves through side reactions. (Fig. 7b) [64]

1.2.3. Carbodiimide Crosslinker Chemistry

By APTES amine-terminated films form the basis of many reactions and open the possibility to various applications, such as the direct attachment of biofunctional molecules by carbodiimide crosslinking chemistry.[65] Here, $-\text{COOH}$ (carboxyl) groups are modified by 3-(Ethyliminomethyleneamino)-N,N-dimethylpropan-1-amine (EDC) and 1-Hydroxy-2,5-pyrrolidinedione (NHS) to form a stable secondary $\text{R}_1-\text{CONH}-\text{R}_2$ (carboxamide) bond with any primary amine.

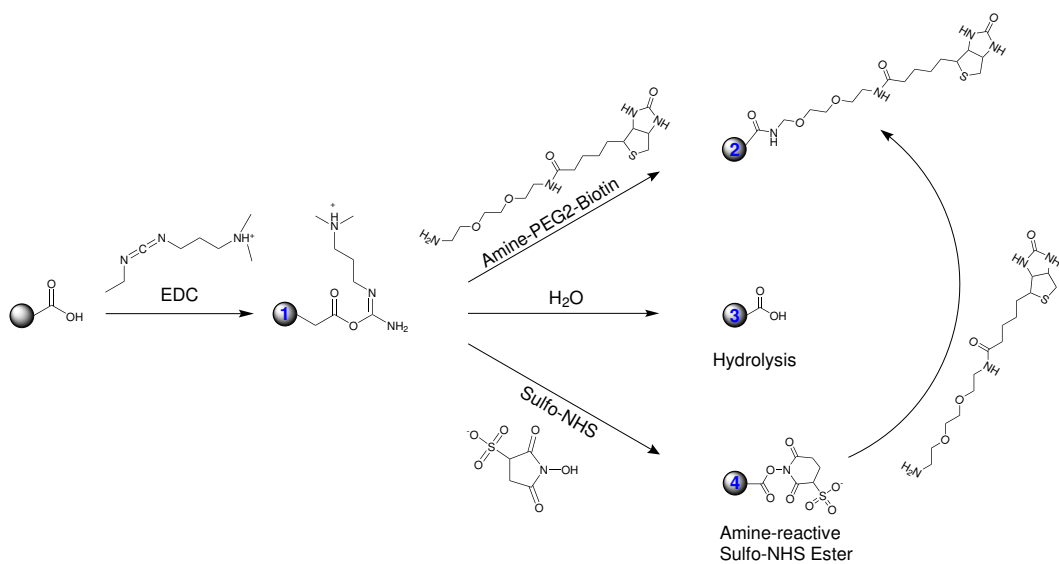


Figure 8: Carboxyl bead modification with EDC/NHS

The carboxyl groups on the bead are activated with EDC to an active O-acylisourea intermediate. This can then either be nucleophilically attacked by a primary amine of the amine-PEG₂-biotin reactant or - due to its instability - hydrolyzed back to a regenerated carboxyl surface. A present NHS-ester can also displace the O-acylisourea to form a considerably more stable intermediate which then itself reacts with any primary amine.

The general reaction mechanism is depicted in Fig. 8 for the example of a particle surface, but it can equivalently be applied to any other modified surface or molecule. The initial carboxyl group is esterified by EDC to an active o-acylisourea intermediate and leaves rapidly upon nucleophilic attack of an amine with release of an iso-urea byproduct. A zero-length amide linkage is formed. (Fig. 8, 1->2) Sulfhydryl and hydroxyl groups also will react with such active esters, but the products of such reactions, thioesters and esters, are relatively unstable compared to an carboxamide bond. (Fig. 8, 1)[65] However, this reactive complex is slow to react with amines and can hydrolyze in aqueous solutions. If the target amine does not find the active carboxyl before it hydrolyzes (Fig. 8, 3), the desired coupling cannot occur. This is especially a problem when the target molecule is in low concentration compared to water, as in the case of protein molecules. Notwithstanding, forming a NHS ester intermediate from the reaction of the hydroxyl group on NHS with the EDC active-ester complex increases the resultant amide bond formation remarkably. (Fig. 8, 4->2) [66]

Another critical point in carbodiimide chemistry is the solubility of the compounds. EDC, NHS and 1-hydroxy-2,5-dioxopyrrolidine-3-sulfonate (sulfo-NHS) are soluble in aqueous and organic solvents. Nevertheless, activation with non-sulfonate NHS decreases water-solubility of the modified carboxylate molecule, while activation with sulfo-NHS preserves or increases its water-solubility by virtue of the charged sulfonate group.[67]

1.2.4. The Biotin-Avidin-System

Until now, the interaction of the homotetrameric protein avidin and its ligand biotin forms one of the strongest known non-covalent bonds in biological systems characterized by a K_d in the range of 10^{-15} M.[68] First isolated from chicken egg white, it became a standard to use in biotechnology when researchers found a similar bacteria protein - streptavidin - in *Streptomyces* strains.[69] However, the charged glycoprotein avidin exhibits unspecific binding in some assays in comparison to streptavidin. Therefor, several companies developed deglycosylated forms of avidin with a neutral isoelectric points to minimize unspecificity. (NeutrAvidin, Extravidin, NeutraLite) In recent studies, a mutant streptavidin called "Traptavidin" exhibited an even 10 times dissociation rate.[70] As discovered in the early 1990s, biotin is bound inside a highly stable β -barrel structure, and stabilized by hydrogen bonds and van der Waals forces.[71] In a unique mechanism, a side group of biotin (valerate) binds to a neighboring monomer of streptavidin and therefor stabilizes the dimer complex intrinsically.[72, 73] From a thermodynamical point-of-view, the interaction of the vitamin and protein is described by a total free binding energy of 300 kJ mol^{-1} to 330 kJ mol^{-1} for a tetrameric protein.[73] All these aspects lead to a significant rupture force for the biotin-release of 250 pN .[74]

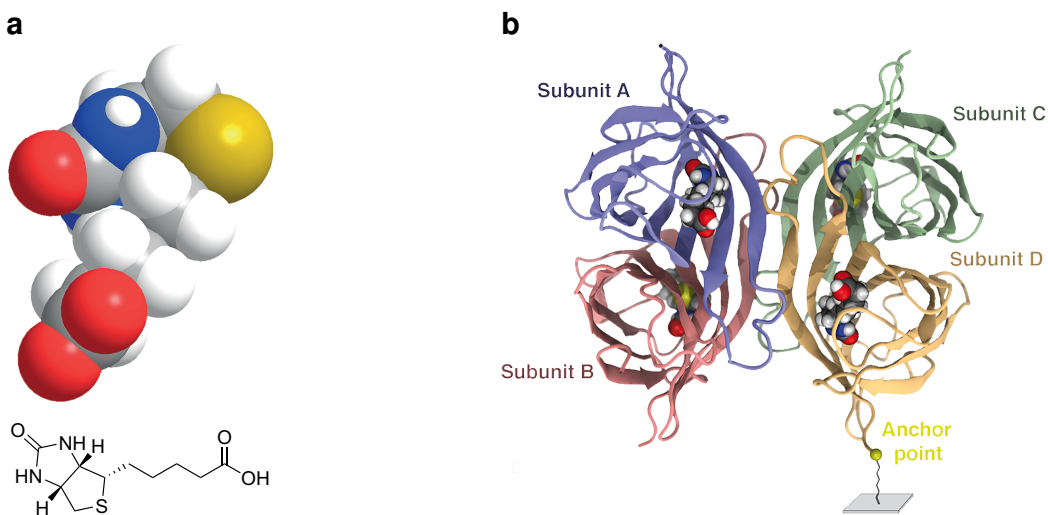


Figure 9: Functional Structures of Biotin and Streptavidin

(a) Two- and three dimensional chemical structure of the biotin molecule. (b) Homotetrameric streptavidin with four subunits and four bound biotin-ligands. The molecule is attached with the anchor point at one terminus to a surface.[75]

1.3. Magnetoresistive Sensing

The measurement system's main component is a GMR-sensor stack with a measured magnetoresistive effect of ~8 %. GMR is a quantum mechanical magnetoresistance effect observed in multilayers composed of alternating ferromagnetic and non-magnetic conductive layers. The driving factor for this resistance is anisotropy of a soft ferromagnetic layer. Two ferromagnetic layers with a thin conducting, non-magnetic spacer in the center build the base of the GMR stack.[76] One ferromagnetic layer has a so called pinned magnetization by exchange coupling, which is insensitive to outer magnetic fields. The second, "easy" layer is soft magnetic. Hence, it modulates its orientation in dependence to small coercive forces. [77]

In the case if both layers are aligned parallel, applying a current to the sensor allows majority charge carriers to pass through the layers with less impact into electrons on either sides. Accordingly, the overall resistance is low compared to another extremum in the antiparallel alignment. The magnetization direction can be controlled, for example, by applying an external magnetic field.[78, 79]

In the present system, GMR stacks were used in a Wheatstone configuration, where two bridges act as a reference for bridge balancing. In front of the sensor, nickel-based chevron patterns act as pre-enrichment for magnetic particles. These structures are driven by an external permanent magnet hence imposing a high flux density gradient on particles. Above these patterns, previously mentioned Si_3N_4 passivation has been deposited in various thicknesses to achieve inertness. On top of the sensor chip, a straight microfluidic channel is mounted to execute flow cytometry experiments.[80, 81]

In order to measure the change in resistance sensitively, the lock-in principle is used. Here, an amplifier extracts signals in a defined frequency band around a reference frequency. This efficiently filters all other frequency components. Thereby a lock-in amplifier performs a multiplication of its input $V_s(t)$ with a reference signal $V_r(t)$ and low-pass filters the result $Z(t)$. In most integrated cases, the reference signal is generated additionally by the lock-in amplifier itself. Using a pure sine wave as reference enables a selective measurement at the fundamental frequency or its harmonics.[82]

At a measurement, $V_s(t)$ is split and separately multiplied with the reference signal and a 90° phase-shifted copy of it. After demodulation, the result is constituted from signal components at the sum and the difference of signal and the reference frequency, ω_s and ω_r , respectively.(Eqs. 3.35 to 3.37) In the resulting signal, the trigonometric functions are Euler transformed and the magnitude $R = \sqrt{X(t)^2 + Y(t)^2}$ acts as measurand. The high frequency compounds are then filtered digitally by a low-pass filter of varying order n to increase signal-to-noise ratio (SNR). As described in Eq. 3.39, a low-pass in

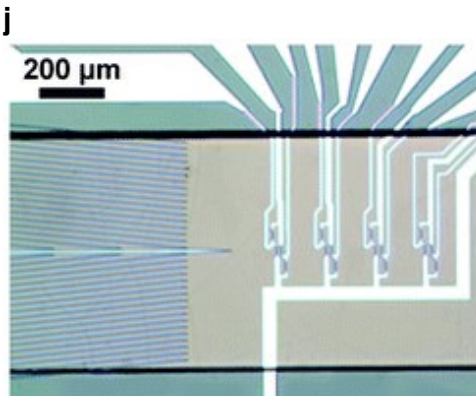
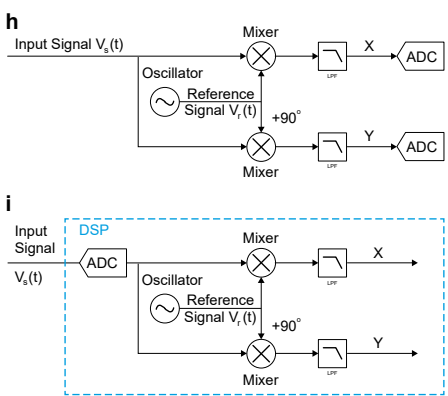
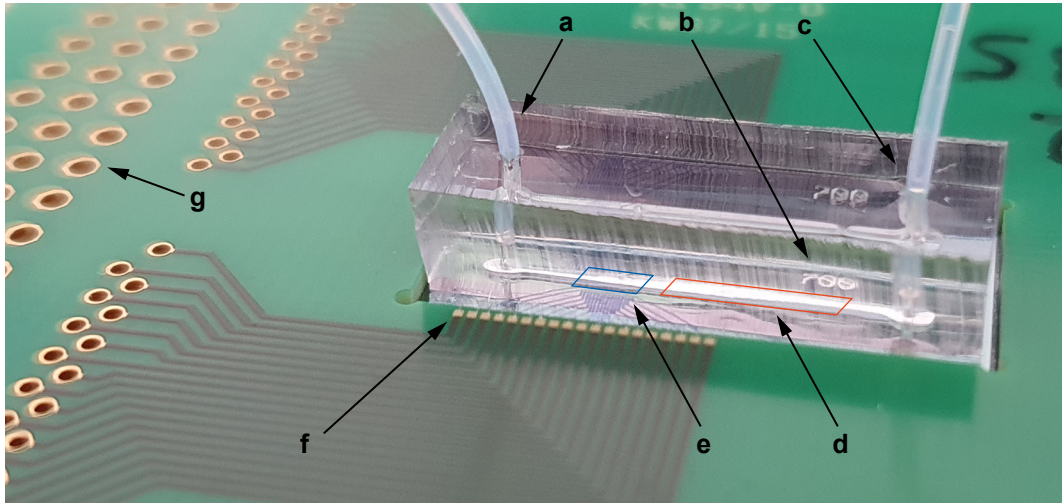


Figure 10: Overview over the MRCyte Sensor Setup

(a) Microfluidic outlet connection to waste reservoir. (b) Imprinted channel width. (c) Microfluidic inlet connection to syringe pump. (d) Magnetophoretic focusing region, not visible in this picture. (e) GMR-sensor region, the supply and bridge balancing traces are visible. (f) Gold bondpad: In order to connect the silicon sensor chip with the breakout printed circuit board (PCB), wedge bonds from the chip pads to the PCB pads are forged. (g) Through hole plating for the connection to the lock-in via jumper cables or a soldered connector plug. (h) Typical signal processing flow of a lock-in. The reference signal $V_r(t)$ is splitted and mixed with the input signal with a phase difference of 0° and 90° . Then, both signals are low-pass filtered and sampled by an analog-to-digital converter (ADC). (i) Accordingly, in a digital signal processing (DSP) device the input signal is digitally converted beforehand, which in turn requires a highly sensitive and fast ADC. In contrast, DSP is more accurate and allows for software-controllable technical opportunities. (j) GMR-sensor bridge circuit inside the microfluidic channel. On the left hand side, magnetophoretic focusing structures are visible. On the right hand side, four Wheatstone bridges on a compliant ground plane can be observed.

the frequency domain can be described by a power series of first-order filters.

$$V_s(t) = \sqrt{2}R \cdot \cos(\omega_s t + \Theta) \quad 3.35$$

$$V_r(t) = \sqrt{2}e^{-i\omega_r t} = \sqrt{2} \cos(\omega_r t) - i\sqrt{2} \sin(\omega_r t) \quad 3.36$$

$$Z(t) = X(t) + iY(t) = V_s(t) \cdot V_r(t) \quad 3.37$$

$$= R \left[e^{i((\omega_z - \omega_r)t + \theta)} + e^{-i[(\omega_z + \omega_r)t + \theta]} \right] \quad 3.38$$

$$H_n(\omega) = H_1(\omega)^n = \left(\frac{1}{1 + i\omega\tau} \right)^n \quad 3.39$$

However, with this measurement principle SNR can not increase infinitely. If the signal strength cannot be increased, the noise has to be reduced or avoided as much as possible. Nevertheless, noise is always caused by different sources in analog signals, for example thermal, shot, and flicker noise. Other sources are of technical origin, as for example ground loops, crosstalk, 50 Hz noise or electromagnetic pick-up. [82]

Now, to characterize a GMR with the lock-in, the easy layer has to be deflected to the full extents. For this, Helmholtz coils impose a high field in the orthogonal direction. The lock-in captures a hysteresis during the sweep from parallel to anti-parallel alignment of the layers at a specific bridge circuit. The steepness hereby indicates the sensitivity of the sensor element in the units V T^{-1} .

2. Results

2.1. Virtual Prototyping of Cell Signals

During the course of this thesis, numerical simulations for the microchannel have been carried out. First, a simulation about the shape of a GMR-sensor signal of cells was performed, where the magnetic momentum was conveyed through magnetic nanoparticles (MNPs) bound to their surface. Second, cell aggregates have been looked at in the same manner with different angles respective to the sensor. Third, both simulations were correlated to a reference dipole, with the equivalent magnetic momentum distributed in the center of mass.

Additionally, the flow and shear field inside the channel was simulated numerically for the channel cross-section as well as for a particle near the walls. A force equilibrium simulation was also established in a basic manner.

Every simulation was captured inside the MATLAB class “MRCyte”, which contains material parameters, constants and the necessary functions for all simulations above.

2.1.1. Numerical investigation of immunomagnetic label density and size on quantitative magnetoresistive sensing of single cells and cell aggregates

In order to mimic a immunomagnetically labeled cell flowing over the sensor half bridge, the planar integral of the respective magnetic flux density (\mathbf{B}) was solved analytically. Here, \mathbf{r}_i specifies the distance vector of a single MNP from the sensor plane. The magnetic flux density was converted to a resistive change \mathbf{R}_{sig} by scaling it with the GMR-sensitivity S and subsequently into a signal voltage \mathbf{V}_{sig} inside the bridge branch.(Eqs. 1.1 to 1.3)

In the numerical approach, MNPs were randomly sampled on a sphere surface with an equivalent diameter of $4\text{ }\mu\text{m}$ or $8\text{ }\mu\text{m}$. Then, the signal was computed from the superposition of every MNP during each timestep. Additionally, the MNP distribution was rotated in every iteration to resemble a rolling motion. The computed signals were then cross-correlated to the signal of a reference flux density \mathbf{B}_{ref} caused by a point-like magnetic momentum located in the geometric center of the same sphere.

$$\mathbf{B}(t) = \sum_{i=1}^N \frac{1}{A_{\text{Sensor}}} \int_{-\frac{l}{2}}^{\frac{l}{2}} \int_{-\frac{w}{2}}^{\frac{w}{2}} \frac{\mu_0}{4\pi} \left(\frac{3\mathbf{r}_i(t) (\mathbf{r}_i(t) \cdot \mathbf{m}_i)}{|\mathbf{r}_i(t)|^5} - \frac{\mathbf{m}_i}{|\mathbf{r}_i(t)|^3} \right) dx dy \quad 1.1$$

$$\mathbf{R}_{sig}(t) = -\mathbf{B}(t) \cdot \frac{S}{100} \cdot R + R \quad 1.2$$

$$\mathbf{V}_{sig}(t) = \frac{\mathbf{R}_{sig}(t)}{R + \mathbf{R}_{sig}(t)} \cdot V_p - \frac{V_p}{2} \quad 1.3$$

By its formula, cross-correlation $R_{xy}(\tau)$ yields a displacement dependent signal through its convolution of the complex conjugated reference signal $\mathbf{V}_{ref}^*(t)$ with the sample signal $\mathbf{V}_{sig}(t + \tau)$. (Eq. 1.4) Therefor, only the maximal correlation of this function was considered in further analyses.

$$\max\{R_{xy}(\tau)\} = \max \left\{ \int_{-\infty}^{\infty} \mathbf{V}_{ref}^*(t) \mathbf{V}_{sig}(t + \tau) dt \right\} \quad 1.4$$

2.1.2. Single Cell Signal

Aim of these simulations is to find a measure of how magnetic labeling of a cell affects signal shape and its subsequent analysis. A single cell with a surface coverage of 5 % to 99 % of a densely packed sphere was loaded randomly with MNPs at different sizes. Then, the previously explained rolling motion over the sensor bridge was simulated with the parameters specified in Table 1. After correlation of the resulting signal voltage to the reference dipole signal (Fig. 11b, with three randomly MNP distributions, the dependency on the coverage was evaluated. As shown in the schematic Fig. 11b, an increase in signal peak amplitude but also in full width at half maximum (FWHM) at growing coverage was expected .

The expected behavior matches the data analysis (Fig. 12). Each two analyzed sphere diameters 4 μm and 8 μm with MNP sizes ranging from 20 nm to 2 μm , show a great standard error of the mean (SEM) at low coverage. This very probably is subjected to

Parameter	Unit	Value	Explanation
w	m	2.0×10^{-6}	GMR width
l	m	30.0×10^{-6}	GMR length
d	m	14.0×10^{-6}	Distance between two sensors
R	Ω	250	GMR Resistance
V_p	mV	100	Supply voltage
$t_{free layer}$	m	7.0×10^{-9}	Thickness of free layer
M	A m^{-1}	2.0×10^4	Volume Magnetization
$V_{noise,rms}$	V	2.5×10^{-6}	Artifical noise
Sim. Space	m	$[-25 \times 10^{-6}, 25 \times 10^{-6}]$	Interval around sensor center

Table 1: Magnetic Simulation Parameters

Constants used inside the framework for the simulation of the magnetic field inside the GMR Wheatstone half bridge. The volume magnetization was adapted according to the simulated particle size.

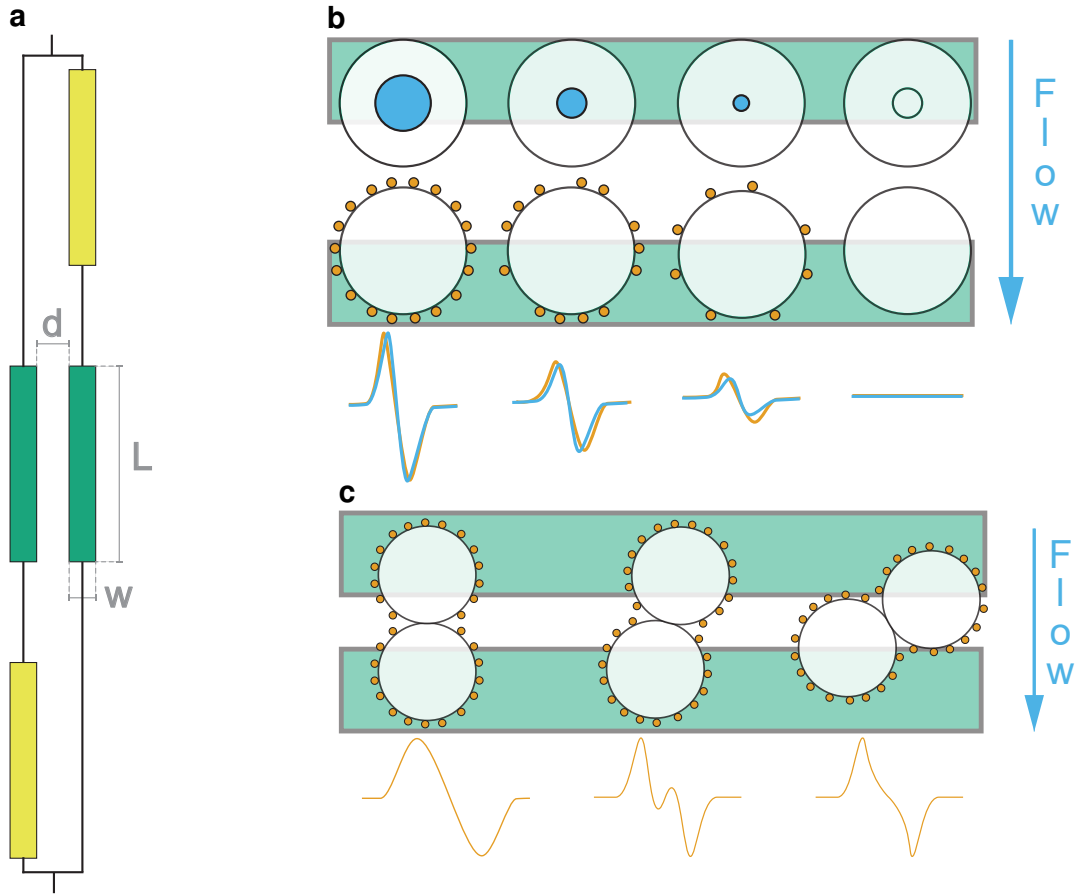


Figure 11: Particle Coverage Simulation

(a) Dimensions of the GMR Wheatstone bridge sensor: Distance d between both variable bridges (green), width w of a GMR-sensor, length L of a sensor. (b) Scheme of single cell simulation: The ideal magnetic dipole in the geometric center of a sphere (●) causes a signal deviation from the real cell signal with magnetic moment distributed on the cell surface. (●) (c) Signal shapes of different angles of two-particle aggregates lead to differing signal shapes.

the momenta of single particles which play a greater individual role and hence influence the signal shape significantly because the overall dipole momentum in the sensor loses homogeneity.

Another observable effect is related to the MNP size. Absolute correlation differs from 20 nm to the ten and hundred fold diameter significantly. This can be related to the magnetic momentum per MNP as it is dependent on the volume - thus r^3 . However, for bigger magnetic particles this does not hold true because the composition changes from pure magnetite to a polymer shell with embedded oxide core at around 150 nm. Nevertheless, larger particles carry also greater magnetic momentum which brings the aforementioned influence of single MNPs into consideration.

Further, the densely packed sphere surface can evidently carry more smaller than larger MNPs. This ranges from 641 600 MNP at 20 nm to 81 at 2 μm for a sphere radius of 4 μm and thus limits the maximum achievable momentum.

In reality, a maximum immunomagnetic label density depends not on the densely packed sphere but rather on the present antigens, and association or dissociation constants. Therefore, a complete saturation coverage is not achievable under physiological condi-

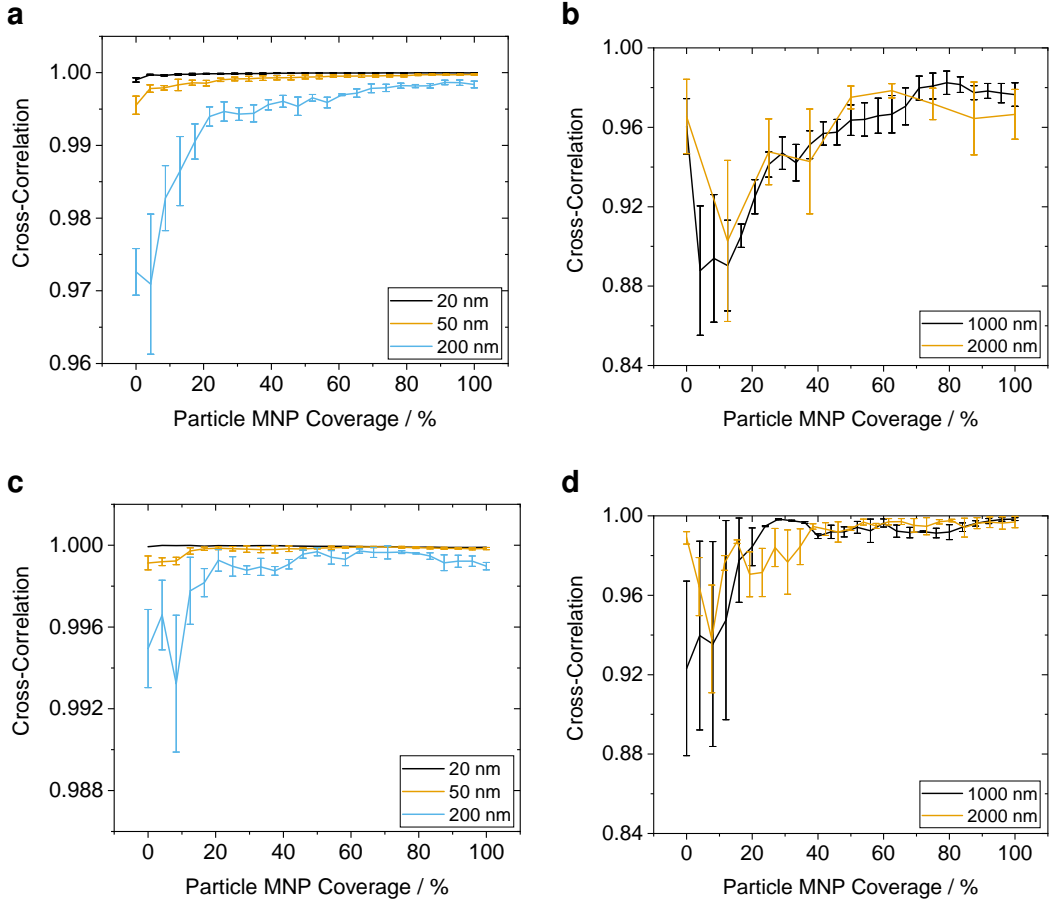


Figure 12: Coverage Dependent Signal Correlation

MNP coverage of a sphere with 4 μm (**a**, **b**) and 8 μm diameter (**c**, **d**) covered by magnetic particles ranging from 20 nm to 2000 nm. A cross-correlation increase which is inversely proportional to the MNP size can be observed.

tions. This leads to the fact that any possible momentum by deposition of 20 nm and 50 nm on a cell surface cannot be resolved from noise by this sensing setup.

Also, it can be seen that the correlation approaches a maximum obtainable value for every MNP size. Referenced for both simulated sphere diameters in Fig. 13a, a inverse proportionality between correlation and MNP diameter is visible. The trend in respective maxima can be attributed to variations in the magnetic momentum, and to coverage inhomogeneity.

Inter-sphere compared, maximum correlation shows also a significant deterioration for higher MNP sizes as the particle diameter itself increases. The relative error between both sizes - as computed in Eq. 1.5 - is depicted in Fig. 13b. Assuming a dependency on the available particle surface and subsequently the fraction which can be occupied by MNPs, a quadratic fit seems appropriate.(Eq. 1.6) The fit indicates probably that a reference dipole cannot be discriminated from a cell at small MNP diameters while the

correlation error becomes nearly constant at great MNPs.

$$\text{Relative Correlation Difference} = 1 - \frac{\max\{\text{Cross-Correlation}(d = 4 \mu\text{m})\}}{\max\{\text{Cross-Correlation}(d = 8 \mu\text{m})\}} \quad 1.5$$

$$\text{Relative Correlation Difference} = -0.385\,32 d_{MNP}^2 + 3.345\,74 d_{MNP} - 8.496\,29 \quad 1.6$$

2.1.3. Cell Aggregates

In another simulation, two 200 nm-MNP-covered spheres were attached to each other in differing angles and simulated flowing over the sensor. Signal similarity to a magnetic dipole in the center of a single reference sphere was computed by cross-correlation. As can be observed in Fig. 14, correlation is identical to a single sphere at low coverage, when the magnetic momentum is high enough to form a uniform magnetic field.

At occupancies greater than 50 %, the two attached cells have to be considered as individual dipoles in superposition and thus show a signal that carries small peaks in the center. This is shown schematically in Fig. 11c. In term, this causes a high signal deviation from the reference and thus a low degree of correlation.

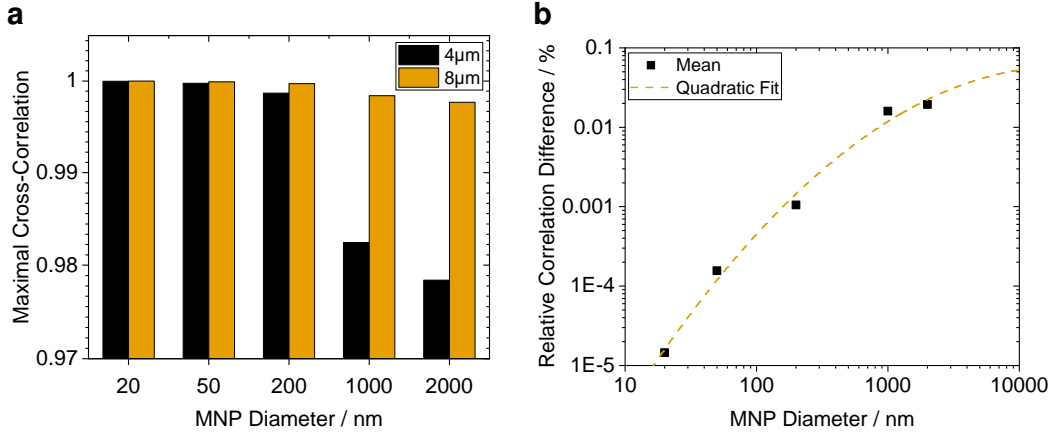


Figure 13: Maximal Cross-Correlation Differences

(a) Mean coverage at 99% for 4 μm and 8 μm spheres. A negative dependency on the MNP size can be explained by the ratio of magnetic momentum per unit surface and its homogeneous distribution across the whole surface.
 (b) Relative correlation error between 4 μm and 8 μm spheres with a quadratic fit. The quadratic behavior could be related to the relative surface area which can be occupied by magnetic momentum. (Adj. $R^2 = 0.99209$)

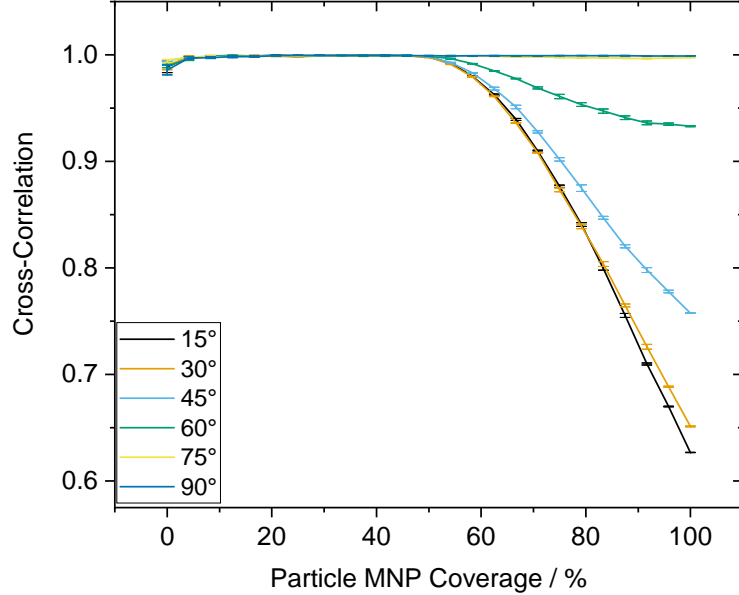


Figure 14: Signal Correlation between Two-Cell Aggregates At Shifting Angles

Two-Sphere aggregates are covered with 200 nm MNPs and simulated flowing over the sensor at differing respective angles. The SEM indicates a difference in cross-correlation of three truly random MNP distributions. For low yaw angles and high coverages, the aggregate's signal reflects rather two single dipoles in superposition than one quite homogeneous dipole. This causes a high signal deviation from the reference and thus a low degree of correlation.

2.2. The MRCyte Simulation Framework

In this work, also an analytical simulation framework that is capable of simulating the synergy of multiple microfluidic effects was developed. The comprehensive framework features magnetic, fluid dynamic and biochemical processes inside the utilized microfluidic channel which act on a particle. Foremost, material parameters were stored inside the “MRCyte” class, which ranged from channel and particle properties to binding and friction constants. Basic velocity, shear and magnetic field computations build the core of the presented program. Additionally, several dimensionless parameters such as the Stokes or Re or particle properties can be computed.

With that, simulations of the fluid dynamics that influence a single microbead as well as force-equilibrium computations for the same bead were carried out.

abilities - Simulation bead
sensor, particle distribu-
on surface, analysis of
Tool data single and dif-
fential, magnetic field perma-

2.2.1. Fluid Fields inside the Microchannel

The simulation framework provided a quantitative generation of the Hagen-Poiseuille flow profile inside the microchannel with the numerical solution of Eq. 1.11. The simulated channel had dimensions ($w \times h \times L$) $700 \mu\text{m} \times 150 \mu\text{m} \times 15800 \mu\text{m}$. The flow rate was adopted to $80 \mu\text{L min}^{-1}$.¹ Tubing as well as time dependent effects were neglected. The simulated flow field (\mathbf{u}) for the whole channel cross-section can be observed in Fig. 15a. Due to the no-slip boundary condition, \mathbf{u} is zero on the margin while the maximum of is reached in the geometric center. Mean fluid velocity ($\bar{\mathbf{u}}$) in the channel ensues $12670.84 \mu\text{m s}^{-1}$.

Conjointly, computation of the flow gradient in vertical direction and scaling with η yield the shear stress field.(Fig. 15c) As the curvature of \mathbf{u} is zero in the channel center and maximal at the edges, the shear stress reaches highest values symmetrically at the horizontal edges of the channel.² Resulting, the net viscous shear $\tau_{viscous} = \frac{\partial u}{\partial z}$ cancels out over the whole channel cross-section.

Additionally, \mathbf{u} and $\tau_{viscous}$ acting on a $8 \mu\text{m}$ diameter bead on the channel bottom were analyzed.(Figs. 15b and 15d) In the proximity of a wall and due to the applied boundary conditions, $\tau_{viscous}$ enclosed by the bead surface is non-linear. Thus, the mean fluid velocity exposed to the bead amounts in $\bar{\mathbf{u}}_p = 2241.59 \mu\text{m s}^{-1}$, whereas $\tau_{viscous,p}$ strains with $4.93 \text{ dyne cm}^{-2}$.

¹ in accordance with the experimentally determined value

² Because the horizontal components of the gradients were neglected graceless

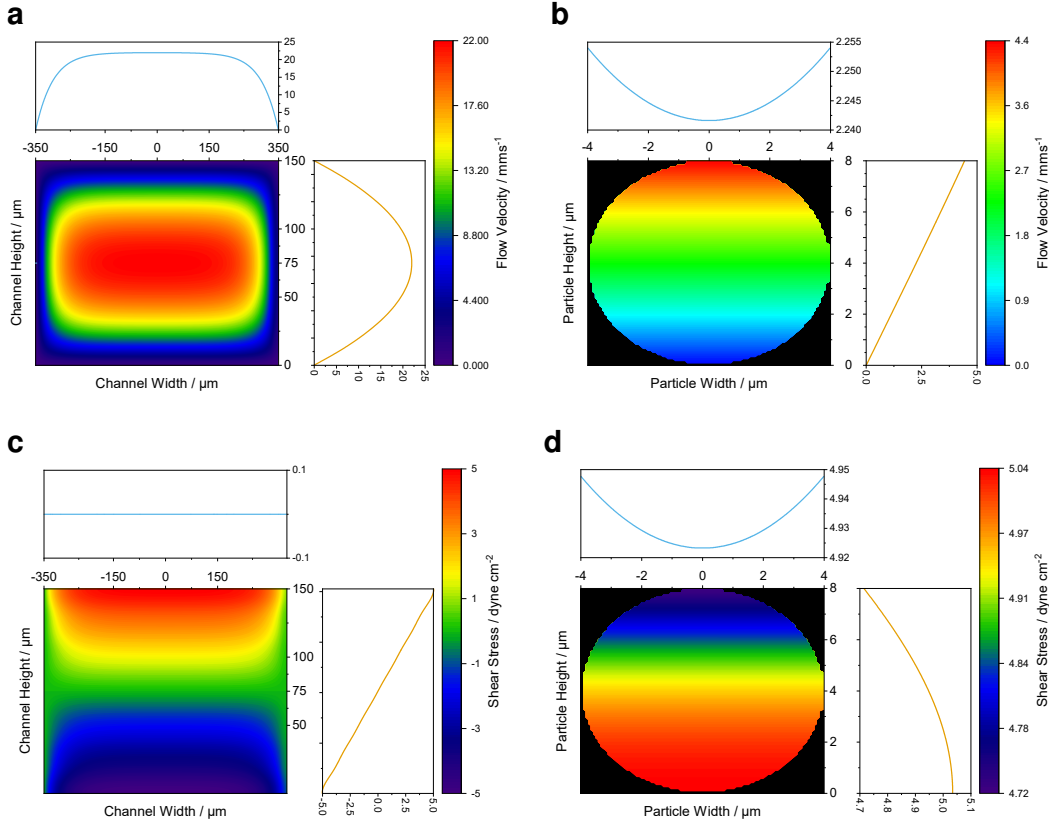


Figure 15: Flow Field and Shear Stress Simulation of the utilized Microchannel

Flow (a) and vertical shear (c) field inside the microchannel with dimensions ($w \times h \times L$) $700 \mu\text{m} \times 150 \mu\text{m} \times 15800 \mu\text{m}$ for a flow rate of $80 \mu\text{L min}^{-1}$ and with neglected tubing effects. The subplots on the right and top side show the mean horizontal and vertical profile in $0 \mu\text{m}$ width and $75 \mu\text{m}$ height, respectively. (vertical: —, horizontal: —) Due to the no-slip condition, the velocity at the walls equals zero and the shear is maximal. The maximum of the Hagen-Poiseuille profile is located in the channel center. Over the cross-section the mean flow velocity \bar{u} equals $12670.83 \mu\text{m s}^{-1}$. Resultingly, the net horizontal viscous shear $\tau_{viscous} = \frac{\partial u}{\partial z}$ cancels out over the whole channel cross-section.

Flow (d) and vertical shear (d) field acting on a $8 \mu\text{m}$ diameter bead on the channel bottom. The mean fluid velocity trapped by the bead profile results in $\bar{u}_p = 2241.59 \mu\text{m s}^{-1}$, whereas the viscous shear strains with $\tau_{viscous} = 4.93 \text{ dyne cm}^{-2}$

2.2.2. Modelling the Force-Equilibrium of a Rolling Bead over a Biofunctionalized Surface

With the supplier's parameters of a 8 μm micromer-M bead (micromod Partikeltechnologie GmbH, Rostock) the corrected drag force on a bead on the bottom of the standard utilized microchannel results in 463.65 pN for 80 $\mu\text{L min}^{-1}$.

If the bead was functionalized with biotin under negligence of the differential equations for the association constants, the number of interacting groups would result in the present surface charges. Surface charge density results in 1 $\mu\text{mol g}^{-1}$ of carboxyl and amine beads as of the supplier's data sheet. Hence, a fully saturated bead is covered in 177 500 biotin molecules.

The streptavidin coverage of the channel floor was modeled in excess over the biotin ligands and penetration depth was estimated by the size of several monolayers of protein. As described by Wu and Voldman [9], an approach of 30 nm is a reasonable quantity. In turn, the surfaces were in contact with 1.51 μm^2 which constitutes 0.75 % of the 8 μm bead surface. This reveals that 1329 biotin molecules can interact with the floor. A summation of the protein-bond force ($\mathbf{F}_{protein}$) at 5 pN to 150 pN per streptavidin-biotin bond yields the resulting adhesion force with a magnitude of 6.7 nN to 199 nN.[74]

The binding force is in the same range as the perpendicular magnetophoretic force caused by the permanent magnet under the sensor chip ($\nabla\mathbf{B} = 10 \text{ T m}^{-1}$) as well as by the nickel-iron chevron structures on the chip ($\nabla\mathbf{B} \approx 5 \text{ kT m}^{-1}$). Clearly, in the near-field approximation the nickel-iron structures dominate \mathbf{F}_{mag} (Eq. 1.22). With the manufacturer given saturation momentum of one particle (1.12 pA m²), the magnetic attraction force eventuates in 5.6 nN.

$$\mathbf{F}_{\parallel} = \mathbf{F}_{drag} - C_{rr} \cdot (\mathbf{F}_{mag} + \mathbf{F}_{protein} + \mathbf{F}_{grav} - \mathbf{F}_{shear}) \quad 2.7$$

$$C_{rr} = \sqrt{\frac{z}{d}} = \sqrt{\frac{30 \text{ nm}}{8 \mu\text{m}}} = 0.0612 \quad 2.8$$

In order to merge this analytic force balance, all remaining forces have to be projected into the direction of Stoke's drag force (\mathbf{F}_{drag}).(Eq. 2.7) This is achieved by the introduction of a rolling resistance factor (C_{rr}) for a perfectly elastic surface.(Eq. 2.8) In a first order approximation, the factor depends only on the approach (z) and the bead diameter (d). However, scientific literature about the rolling resistance of microbeads on microfluidic or protein covered surfaces does not exist yet to confirm this macroscopic factor for the microscale.

Scaling all orthogonal forces to the Stoke's drag force with C_{rr} yields a net positive result (154.08 pN) for an unfunctionalized surface ($\mathbf{F}_{protein} = 0$) which indicates a rolling

motion in flow direction. Notwithstanding, above a critical interaction number of 503 to 16 biotin-streptavidin bonds - for the respective release forces of 5 pN to 150 pN per linkage - the particle resists Stoke's drag force and adheres to the surface.

This behavior will be exploited in further measurements for "bead loss experiments" in order to measure a concentration difference with different degrees of biotinylated beads.

2.3. Reference Bead Surface Functionalization

After simulation of their respective coverages, biotin was titrated on 8 µm reference beads with two different surface terminations in order to selectively bind MNPs with the counter-agent streptavidin to the surface. First, amine-microbeads were modified by sulfo-NHS-biotin. Second, carboxyl-beads were coated by amine-PEG₂-biotin via EDC-NHS-activation. On the same beads Anti-IgG1-PE antibodies were titrated after the same coupling chemistry.

Subsequently, biotin-coated beads were analyzed in the flow cytometer in the by staining with Atto-488 (Ex: 500 nm, Em: 520 nm) coupled streptavidin. The antibody was already industrially modified with phycoerythrin (PE) and measured at 488 nm excitation and 585 nm emission wavelength. The gating was standardized by the strategy found in ??, ???. Subsequently, the median fluorescence intensity (MFI) was computed and fitted with a Hill-function.(??) Stability of carboxylated and aminated beads and subsequently their respective modification protocols was evaluated for 12 days.

2.3.1. Amine-Surface Biotinylation

As first approach, polystyrene copolymer microbeads with 8 µm diameter were functionalized by (sulfo-)NHS-biotin after a standard protocol. A titration of the biotin reactant yielded a varying surface coverage as shown in Fig. 17a. During this one-pot-reaction, the water-soluble sulfo-NHS-biotin forms an amide linkage with the primary amine and 1-hydroxy-2,5-dioxopyrrolidine-3-sulfonate splits off as byproduct.

As can be seen from the SEM error-bars from the plot 17a, which were constructed from three true biological replicates, this process is highly reproducible. Therefore, an surface coverage in different grades of biotinylation could be obtained accurately with a adjusted coefficient of determination (adj. R^2) of 0.981 for the resulting Hill fit (- - -).

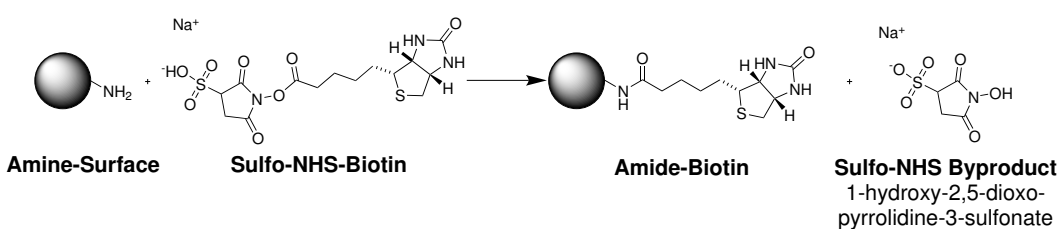


Figure 16: Amine Bead Modification with Sulfo-NHS-Biotin

An amine terminated bead brought into reaction with sulfo-NHS-biotin. Both form an amide linkage and bind biotin covalently to the surface. As byproduct the sulfo-NHS-ester splits off.

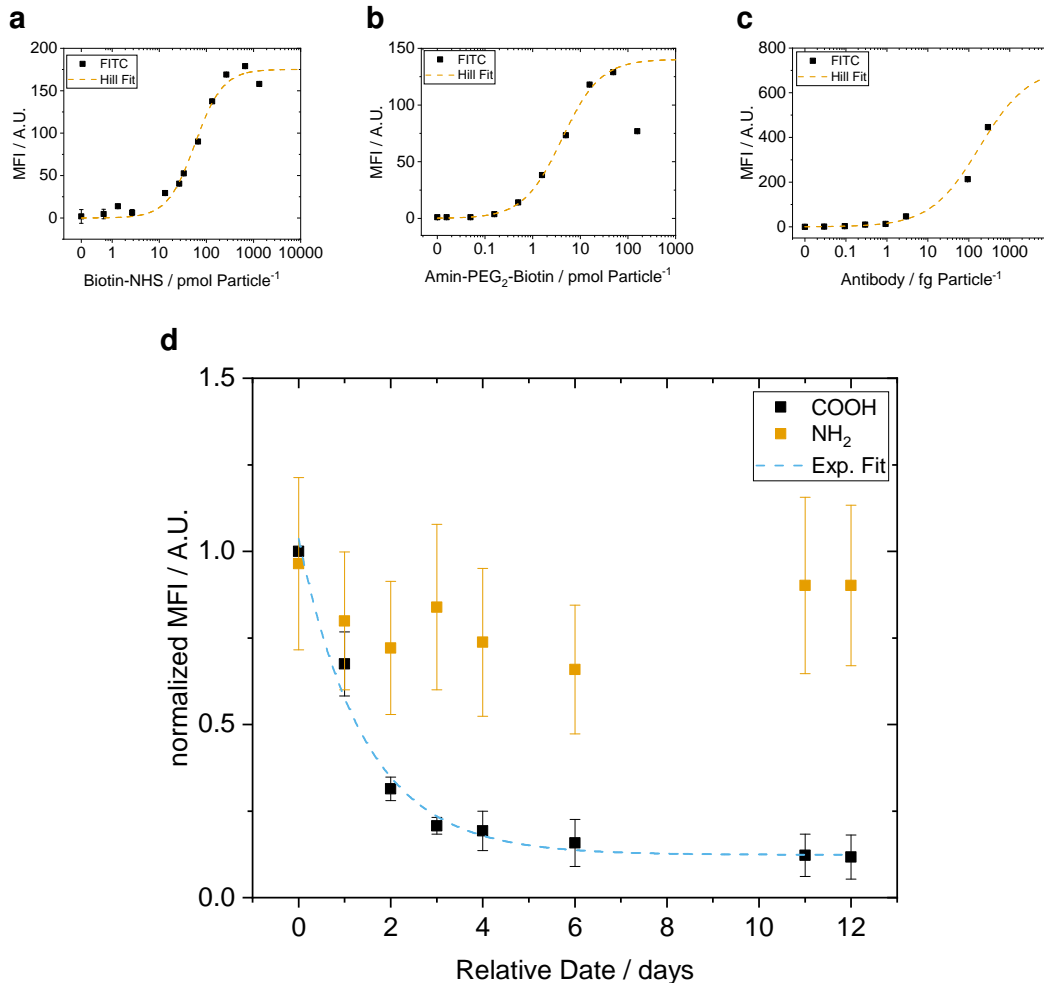


Figure 17: Titration of Biofunctional Molecules on 8 μm Particles

Titration curves of NHS-biotin (a), Amin-PEG₂-Biotin (b), and Anti-IgG1 (c) with their respective Hill fits. The corresponding fit parameters as well as the goodness factor are shown in Table 2a. (d) Stability analysis of functionalized carboxyl and amine beads over 12 days. The carboxylate particles show an exponential decrease with a half-life of 1.43 days as determined by the exponential fit. The respective parameters are shown in Table 2b.

a				b	
Param.	Hill 17a	Hill 17b	Hill 17c	Param.	Exp. 17d
V_{max}	175.216 19	140.391 53	713.836 43	A	0.912 63
k	57.367 13	4.126 61	182.830 11	τ_{decay}	1.425 57
n	1.474 88	1.074 93	0.724 58	y_0	0.123 69
Adj. R^2	0.981 21	0.997 22	0.992 26	Adj. R^2	0.966 55

Table 2: Fit Parameters of Biotinylation

(a) Coefficients for the Hill fits in Figs. 17a to 17c (b) Exponential fit coefficients for the stability analysis in Fig. 17d

Carboxylate-Surface Functionalization

In a second approach, particles with opposite partial surface charge, mediated through carboxyl groups, have been functionalized. In turn, particles were pre-activated in EDC and NHS in 2-(N-morpholino)ethanesulfonic acid (MES)/MES buffer with Tween 20 (MEST) buffer. There are two distinct reasons for the usage of MES based buffers rather than phosphate buffered saline (PBS) or MACS running buffer (MACS). First, EDC has its reactive maximum at pH 5 to 6. Second, buffers containing primary amines (TRIS / glycine) or carboxyls (acetate / citrate) will quench the reaction and therefore limit the efficacy.

Afterwards, the beads were washed carefully and incubated with amine-PEG₂-biotin. Here, poly(oxyethylene) (PEG) indicates a hydrophilic spacer arm between both functional groups and in this case has length of a two units. The full functionalization procedure is explained in more detail in Fig. 8.

As shown in Fig. 17b, particles were functionalized equally compared to carboxamide surfaces. However, the stability of carboxyl particles yields a half-life of 1.43 days in a continuous measurement over 12 days with a subsequent exponential fit. Additionally, both procedures show an outlier at high concentrations which could not be explained during the course of this thesis.

Third, carboxylated particles have been also functionalized with the Anti-IgG1-PE antibody. Again, a Hill-shaped titration curve was achieved, but due to the costly reagent a saturated surface coverage was not reached. (Fig. 17c)

Therefor, the fit curve has to be interpreted cautiously. Although it converged and represents the data with an adj. R^2 of 99.2 %, the goodness of fit determined by the reduced χ^2 statistic results in a value of 278.1 which indicates an underestimation of the error variance.

2.4. Concentration Measurements in MRCyte

Driving factor for the concentration measurement is the absolute count of immunomagnetically labeled cells in diluted or whole blood which is not possible in today's optics-based devices due to the excess of RBCs.[83] Therefore, with the in Sec. 1.3 described sensor setup, absolute concentrations of magnetic reference beads were attempted to measure.

Consequently, beads with acrylate surface were pumped through a microfluidic channel with a permanent magnet underneath. The magnet drew every magnetic particle to the ground, where they were focused on the sensor bridge and subsequently measured there. From the received signal several parameters such as peak amplitudes, locations, zero-crossings, and relative distances between each other were computed.(Fig. 18) Especially for the concentration measurement a correct detection of bead signals from the noisy stream or from a superposition of multiple, simultaneously measured particles was critical. The related error sources and countermeasures will be elaborated in Sec. 2.4.1.

By measuring the absolute concentration with a commercially available flow cytometer (MacsQuant 10, Miltenyi), a reference bead count was established. In a pre-test, beads were taken directly from the microcentrifuge tube, after pumping through a syringe, and after pumping through a syringe with 10 cm of connected tubing (ID 0.5 mm, RS Chemicals). Afterwards, they were counted in the flow cytometer in equal volumes. Additionally, two different buffers - MACS and PBS - and two different surface terminations were used. Both buffers are based on phosphate buffered saline (PBS). Notwithstanding MACS contains 2,2',2'',2'''-(ethane-1,2-diyl)dinitrilo)tetraacetic acid (EDTA) as chelator for divalent ions, Tween 20 - a non-ionic surfactant -, and an azide-based stabilizer. Hence, the wetting of surfaces and the electrostatic interactions of these buffers differ. The same properties were varied on the bead surface by choosing acrylate- and biotin-terminated beads.

In Fig. 19, a trend (without statistical confidence) can be observed that shows a decrease in particle counts after every additional surface which beads could potentially interact with. In term, a correct count in absolute numbers seems out of range. However, a calibration of the system with the flow profile inside the channel to compensate for losses subjected to connectors and magnetic enrichment structures was carried out successfully.

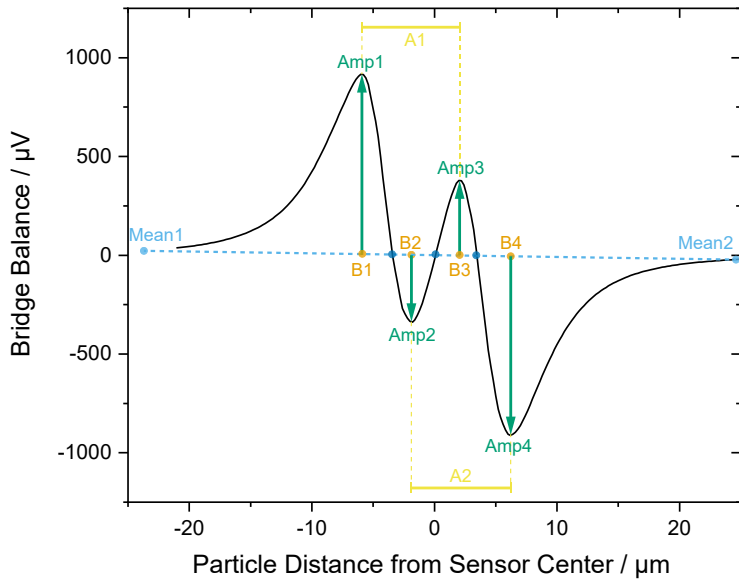


Figure 18: Example Signal of Magnetic Measurement

Signals generated from the Wheatstone bridge sensor setup feature a certain shape which allows for several measures. In case the overall signal stream carries a constant or linear offset, it is scaled to the means before and after the detected peak pattern. (Mean1, Mean2) The x- and y-positions of each peak are denominated by B1-4 and Amp1-4, respectively. The crossings of the signal through the linear connection of both means are denominated by n1-3 (in the figure by ●). Further, the difference between the equally oriented peaks B3-B1 and B4-B2 give a measure for the homogeneous movement of the measured object and are called A1 and A2 each. From these values the overall velocity v can be approximated because the GMR bridge distance (d_{GMR}) and sampling frequency (f_s) is fixed precisely. Analogously, the magnetic diameter of a dipole is computed by the mean of the differences B2-B1 and B4-B3.

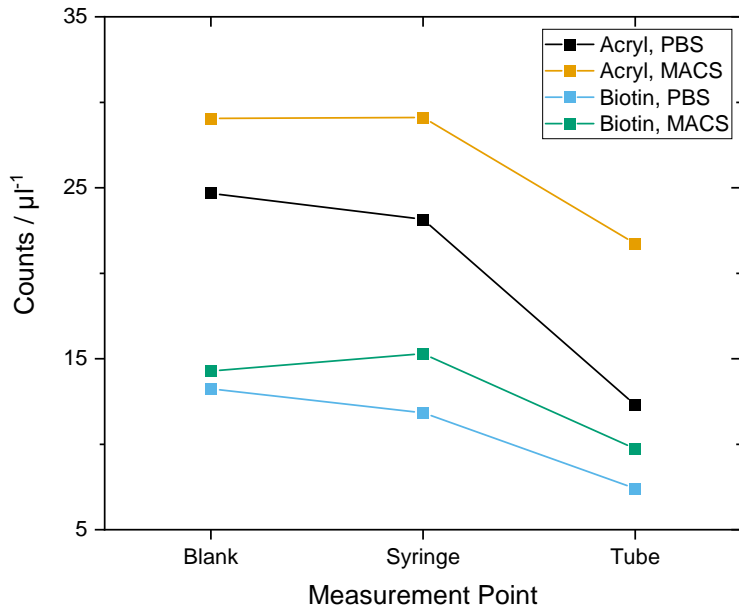


Figure 19: Bead Loss Evaluation in Connectors

Bead concentrations measured in equal volumes in the flow cytometer after being pumped through a syringe or a syringe with connected tubing. The blank sample was measured directly from the stock solution. Additionally, electrostatic and surface tension related effects were resolved by the usage of different buffers and bead surfaces.

2.4.1. Measurement Error Sources and Calibration of Flow Field

In order to account for the bead losses due to the tubing connectors, the Hagen-Poiseuille flow profile, and magnetophoretic enrichment structures, the measured bead concentration was corrected in two different approaches.(Eq. 4.9) On the one hand side, the typical assay correction to the ground truth by a constant linear fit correction factor (C_{const}) computed from the blank population was established. On the other side, a velocity correction factor ($C_{velocity}$) compared the mean fluid velocity (\bar{u}) to the bead velocity (v_c).

$$c_{beads, expected} = c_{beads, measured} \cdot C \quad 4.9$$

The C_{const} relates a reference count in the optical flow cytometer to the measurement in the magnetic flow cytometer.(Eq. 4.10) Equally-adjusted bead concentrations in the samples allow for a correction to the reference system. However, for an assay usage the initial concentration of beads either has to be known precisely or has to be irrelevant, for example in regards of a standardized measurement procedure. Besides, C_{const} provides a reliable and generalizable option for correction.

$$C_{const} = \frac{c_{beads, standard\ procedure}}{c_{beads, MRCyte}} \quad 4.10$$

$$v_c = 2 d_{gmr} \frac{f_s}{n_3 - n_1} \quad 4.11$$

$$C_{velocity} = \frac{\bar{u}}{v_c} = \frac{Q}{A \cdot v_c} \quad 4.12$$

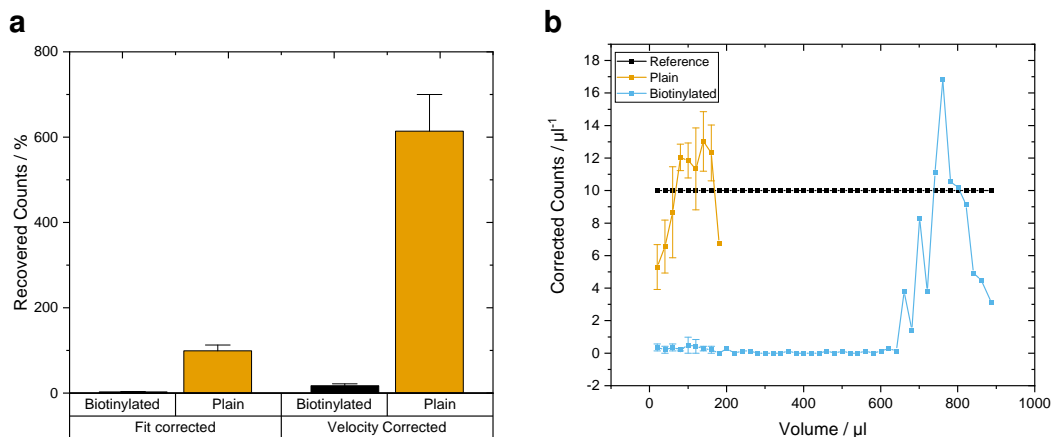


Figure 20: Error Sources in Concentration Measurements

(a) Robustness evaluation of the both correction factors C_{const} and $C_{velocity}$ for protein coated surfaces. The mean and SEM of plain and biotinylated measurements show a high deviation from physically reasonable expectations when corrected for the velocity (right). In contrast, C_{const} can intrinsically correct only well below 100 %. **(b)** Mean and SEM of a fit-corrected bead capture experiment with several error sources. Initially, the magnetophoretic structures have to be filled and thus decrease the plain count for the first 100 μl . (—) Additionally, the high deviation offsets the correction factor so that the stable measurement from 100 μl to 200 μl lies now above the ideal reference. In contrast, the biotinylated beads are captured by the surface functionalization and hence a very low concentration is measured. However, a steep rise with pulsations can be observed when the surface is saturated with beads and the particles begin to flow over the sensor in bursts. (—) The abrupt decline to the end of the measured volume is most probably related to sedimentation effects inside the emptying syringe.

The $C_{velocity}$ relates the effective particle velocity to the total fluid velocity in order to eradicate flow profile provoked effects.(Eq. 4.12) Whereas \bar{v} was determined by flow rate (Q) through a cross-sectional area (A) of the channel, v_c was analyzed from the measured signal stream. Here, the intrinsic GMR bridge distance (d_{GMR}) was divided by the time difference where the bead passed exactly over a GMR-element.(Eq. 4.11) These specific timepoints are visible as dimensionless zero-crossings n_1 and n_3 in the signal and can be converted by scaling with the sampling frequency (f_s) into the time domain.

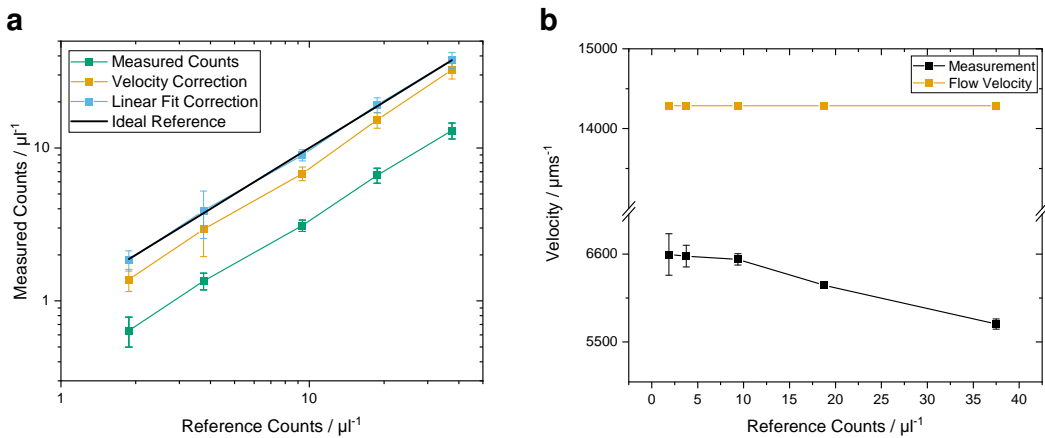


Figure 21: Absolute Concentration Measurements

(a) Mean and standard deviation of the concentration measurement from three independent measurements. The uncorrected measurement shows a highly reproducible and linear count over the dynamic range of almost two decades. (—■—) The ideal reference from the flow cytometer is depicted in (—). Correction with $C_{velocity}$ (—□—) yields at a factor of 2.261 09 which is 21.7 % more imprecise than C_{const} at $2.888\ 33 \pm 0.080\ 75$. (—△—) (b) Mean and SEM of the v_c estimation from the signal. For higher concentrations, the measured velocity becomes inaccurate thus distorts the correction factor.

However, if the bead velocity is not solely dependent on fluid dynamic effects - especially in the light of surface functionalizations - $C_{velocity}$ can not be applied to experiments robustly. This is depicted in a sample experiment with a protein covered surface in Fig. 21a. By definition, the C_{const} can not be well above than 100 % whereas the count correction by $C_{velocity}$ differs by 600 % through variations in the velocity measurement.

An adaptation of these corrections to real measurements are depicted in Fig. 21. In a measurement where $300\ \mu\text{L}$ were dispensed into the magnetic flow cytometer with a defined particle concentration the counts were analyzed and corrected according to above. This time, the channel had a cross-section of $700\ \mu\text{m} \times 50\ \mu\text{m}$ ($w \times h$) and Q was set to $30\ \mu\text{L}\ \text{min}^{-1}$.

Apart from a reproducible count over the dynamic range of almost two decades, both correction factors ameliorated the present data. C_{const} amounted in an optimum 2.89 ± 0.08 while $C_{velocity}$ centered around a mean of 2.26. Consequently, the velocity correction was misguided by 21.7 % for the advantage of requiring no *a priori* knowledge about

the measurement.

Another peculiarity of $C_{velocity}$ can be observed in Fig. 21b. While the analyzed velocity is stable for less than $10 \mu\text{L}^{-1}$, a linear decrease is visible for higher concentrations. This is a consequence when signals of beads start overlapping if these are flowing over the sensor in a close vicinity. Hence, the disturbed signal sensitizes the parameter reconstruction to errors such as false peak-identification.

2.4.2. Concentration Measurement in Diluted Whole Blood

The same concentration measurements from before were now carried out in whole blood samples. Here, the reference count can be attained only below the experimentally determined critical concentration around $10 \mu\text{L}^{-1}$. (Fig. 22) An insignificant discrepancy could be perceived in different volumetric blood to buffer dilutions of 1:1 and 1:20, respectively. This provides evidence for the measurement's independence from the blood concentration in buffer.

However, a significant difference between counts was discovered between a $150 \mu\text{m}$ high channel, where $C_{velocity}$ can be determined accurately, and a $50 \mu\text{m}$ high channel, where the correction yields a great error to the reference. This may be subjected to an increased probability of collisions from beads with blood cells and hence a decreased velocity which in turn leads to a higher correction factor. Another explanation approach could be the transition from *Newtonian* to *Non-Newtonian* fluid dynamics in smaller cross-sections, which could likewise be influenced by the Fåræus effects mentioned in Sec. 1.1.3.

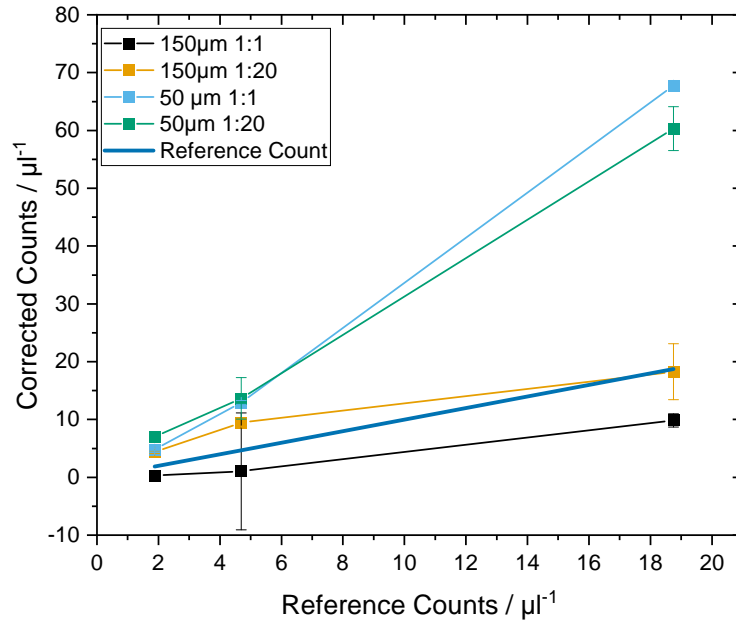


Figure 22: Absolute Concentration Measurement in Blood Samples Under Varying Channel Height
Velocity corrected concentration measurements for two different blood dilutions and channel heights. While $C_{velocity}$ works for high channels in all tested concentrations, it does not work for high concentrations in $50 \mu\text{m}$ high channels. This is probably a result of bead-cell collisions and the resulting path interruption.

2.4.3. Surface Magnetization of Biofunctionalized Beads

Here, the previously surface-modified polystyrene beads were magnetized with MNPs and counted in the magnetic flow cytometer. Originally, four different magnetic nanoparticles have been tested. Albeit, both nanomag-D-spio 100 nm (micromod Partikeltechnologie GmbH, Rostock) and dynabeads MyOne Streptavidin C1 1 μm (ThermoFisher scientific, Waltham, USA) showed inconclusive results and are omitted in the latter.

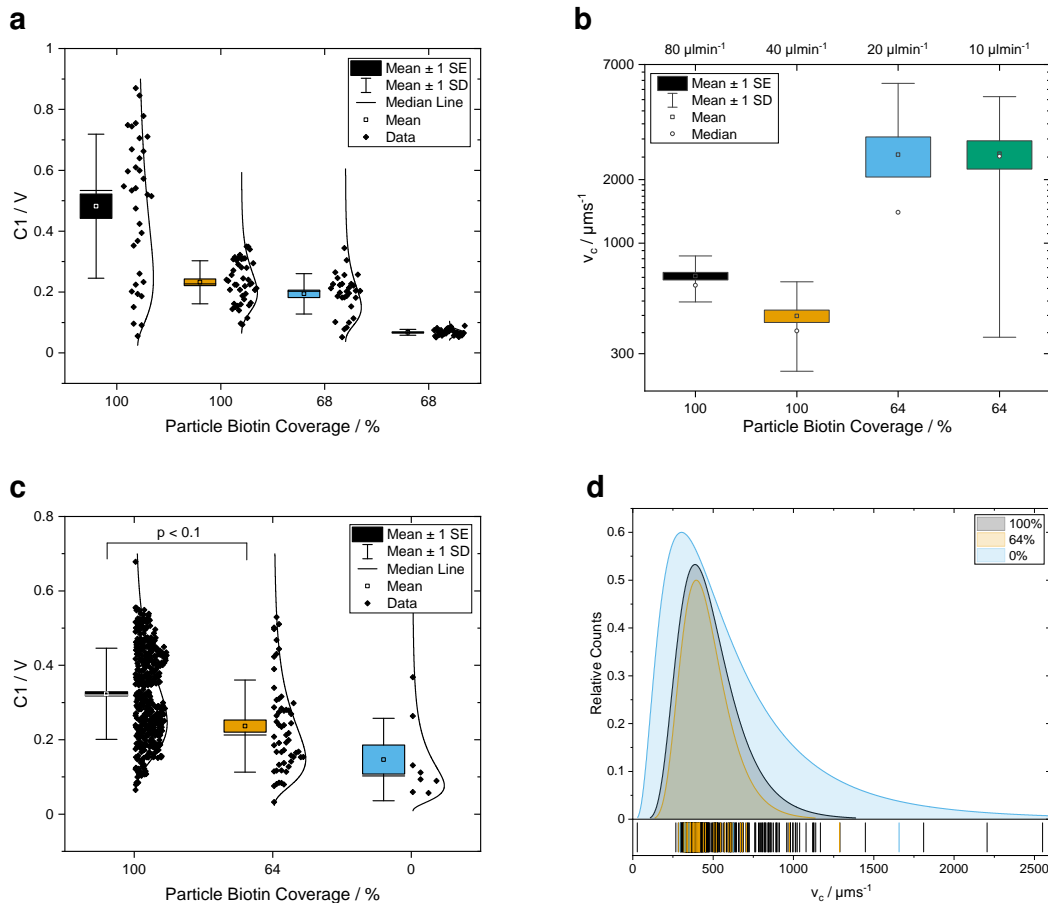


Figure 23: Bead Coverage Assay with Magnetic Streptavidin Nanoparticles

Magnetic flow cytometry data from 8 μm polystyrene sphere which were biotinylated in different degrees and subsequently coated with BNF-Dextran-redF-streptavidin 100 nm MNPs (a,b) or SV0050 50 nm streptavidin MNPs (c,d). (a) Signal amplitude of the counts with various flow rates 1. 80 $\mu\text{L min}^{-1}$ 2. 40 $\mu\text{L min}^{-1}$ 3. 20 $\mu\text{L min}^{-1}$ 4. 10 $\mu\text{L min}^{-1}$ (b) Reconstructed velocities of the respective populations. The 100% biotinylation shows plausible velocities, whereas the 68 % sample can either be considered as noisy background or very weakly magnetized particles. (c) Signal amplitude with 80 $\mu\text{L min}^{-1}$. A correlation between biotinylation degree and magnetic momentum can be assumed at a p-value $p < 0.1$ (d) Velocity distributions of the samples. As postulated, the mean velocities do not differ, moreover, are enveloped by the blank sample.

First, BNF-Dextran-redF-streptavidin 100 nm MNPs (micromod Partikeltechnologie GmbH, Rostock) were attached to the non-magnetic beads after the protocol in ???. Then, the magnetizability was examined qualitatively in a magnet stand. Particles were considered “magnetically labeled” if a pellet was visible after 10 min. Afterwards, the concentrations were measured with the optical flow cytometer and adjusted to $10 \pm 1 \mu\text{L}^{-1}$

accordingly.

The subsequent measurement of 300 μL in the magnetic flow cytometer is shown in Fig. 23. In Fig. 23a the peak difference C1 (= Amp2 - Amp1, Fig. 18) is presented against the biotinylation degree. Independent experiments of 100 % and 68 % biotinylation show a certain amplitude difference. The respective fluid and particle velocities in Fig. 23b provide an explanation for this behavior. The fluid velocity had to be adapted during the course of the experiments from 80 $\mu\text{L min}^{-1}$ to 10 $\mu\text{L min}^{-1}$ in order to receive stable counts.

Keeping this in mind leads to the fact that - although only two biotinylation coverages were measured - four distinct magnetizations are represented here. Both 100 % samples show slow but plausible velocities and can therefore be correlated with differing magnetic momentum. Beads with 68 % show an exceptional velocity and can hence either be considered as noisy background or a very weakly magnetized particles that are not pulled to the channel bottom completely. This could also explain the decline in C1 which is also a measure for magnetic dipole moment.

Second, SV0050 50 nm streptavidin MNPs (OceanNanotech, San Diego, USA) were deposited after the equal procedure on 8 μm polystyrene beads. These experiments show the expected result of declining peak amplitude at lower biotinylation and constant velocity throughout. (Figs. 23d and 23e) At a p-value smaller than 10 %, the high populations differ significantly from each other while the log-normal fits match the histograms with a adj. R^2 of 0.94.

Two hypotheses can be drawn now from this result. On the one side, OceanNanotech MNPs could posses more magnetic momentum per particle, which favors the robust measurement. On the other side, streptavidin or MNP size could influence the saturation of all available biotin sites of the particle.

2.4.4. Count Stability

In this section, the results of beads rolling a neutravidin-covered channel surface will be discussed. In order to measure the interaction properties diligently, beads were functionalized with biotin at several saturation degrees ranging from 0 % to 100 % total coverage of the available surface charges. Measurements for absolute counts as well as their time stability were carried out at 80 $\mu\text{L min}^{-1}$ in a microchannel with cross-section 700 $\mu\text{m} \times 150 \mu\text{m}$ (w x h). Fig. 24a shows the absolute, linearly corrected counts determined by the magnetic flow cytometer, with a defined particle concentration of 7.8 μL^{-1} to 10 μL^{-1} . Clearly, a significant yes-no answer can be established by fully- vs. non-functionalized beads. Also, this measurement demonstrates high reproducibility with three different chip setups and measurement days. For approximately $\frac{2}{3}$ biotinylated beads, a gradation in counts can also be observed. However, due to the instability of the channel surface over the course of many sequential measurements, additional ex-

periments have to be conducted to reinforce these results.

An evaluation of the time-domain distribution of the counted beads shows a very stable baseline for fully biotinylated beads with a recovery in the single digit range per unit volume. In the negative control of unbiotinylated beads, also a noisy mean count around 100 % can be observed.³

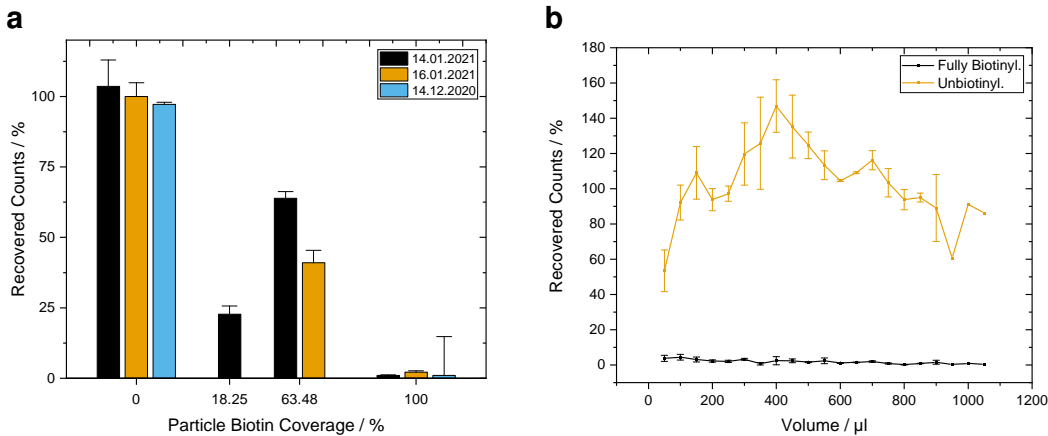


Figure 24: Reproducibility of Concentration Measurements with Saturated Neutravidin Surfaces

Biological replicates of concentration measurements with the magnetic flow cytometer. The channel surface was modified with 1 mg mL^{-1} neutravidin over night. (a) Mean and SEM of C_{const} adjusted counts for various biotinylation degrees. (b) Time series of the mean from the three measurements on the left. Biotin-beads are captured completely, thus very few counts are detected. (—) The unbiotinylated sample shows the initial ascent due to the in Sec. 2.4.1 discussed error which is related to the filling of the magnetophoretic structures. (—)

something about velocity?

³ The shown data corresponds to the mean of three measurements from Fig. 24a

2.4.5. Differential Counting Setup

With regard to the necessity of correction factors in order to resolve the ground truth of a concentration measurement, a different magnetic flow cytometer setup has been evaluated. Here, two fully assembled sensors with PCBs were stacked on top of each other and connected in series which was expected to yield two beneficial effects.

First, one permanent magnet underneath the lower sensor chip should supply both chips with enough gradient field to pull beads to the respective channel bottom. Second, simultaneous signal acquisition should act on the one side as a time-of-flight detector with a relatively long transport distance and on the other side, a differential concentration measurement was envisioned between both chips. Therefor, the hypothetical optimum parameter set could be reached when the relative concentration measurement yielded identity:

$$\frac{c_{\text{top sensor}}}{c_{\text{bottom sensor}}} = 1 \quad 4.13$$

The system comprises of two separately assembled sensor PCBs with nylon spacers between the positional screws.(Fig. 25) A 3 mm hole was drilled into the top PCB carefully between the strip lines to minimize the tubing length from the top chip outlet to the bottom chip inlet. After the build-up of the differential counting system,⁴ the hysteresis of both sensor elements was maximized for sensitivity and the concentration was measured against a reference from the optical flow cytometer.

Sensitivity Calibration

Initially, the permanent magnet was adjusted in three linear directions in order to maximize the magnetic sensitivity of both Wheatstone bridges. Schematically, this can be envisioned as a placement of the whole top as well as the whole bottom bridge configuration into the operational range of the magnet, which is indicated by the blue triangle.

Then, the hysteresis of both outermost and one centered sensor was optimized for their full coverage and sensitivity. The recorded values for a sole optimization of the top or bottom sensor array with a height variation of the utilized nylon spacers are shown in Figs. 25b and 25c. Apparently, the optimized sensor exhibits a monotonously higher magneto-resistive effect (MR effect) than the disregarded bridge. Nevertheless, the complete sensor setup features a MR effect well above 7.2% which is acceptable both for measuring immunomagnetically labeled cells and magnetic microbeads. Furthermore, the homogeneity of the interspersing magnetic field can be monitored in the triangular shape of every acquired curve in the sensitivity plots. As the field vectors of \mathbf{B} start to disperse at the outsides of the illustrated blue area in Fig. 25c, the outer sensor regions are not located completely inside a uniform field and get distracted by non-perpendicular field components.

Additionally, no influence of any spacer height could be discovered. The difference in

⁴ as described in ??

MR effect varied insignificantly in $0.14 \pm 0.60\%$ of MR effect.

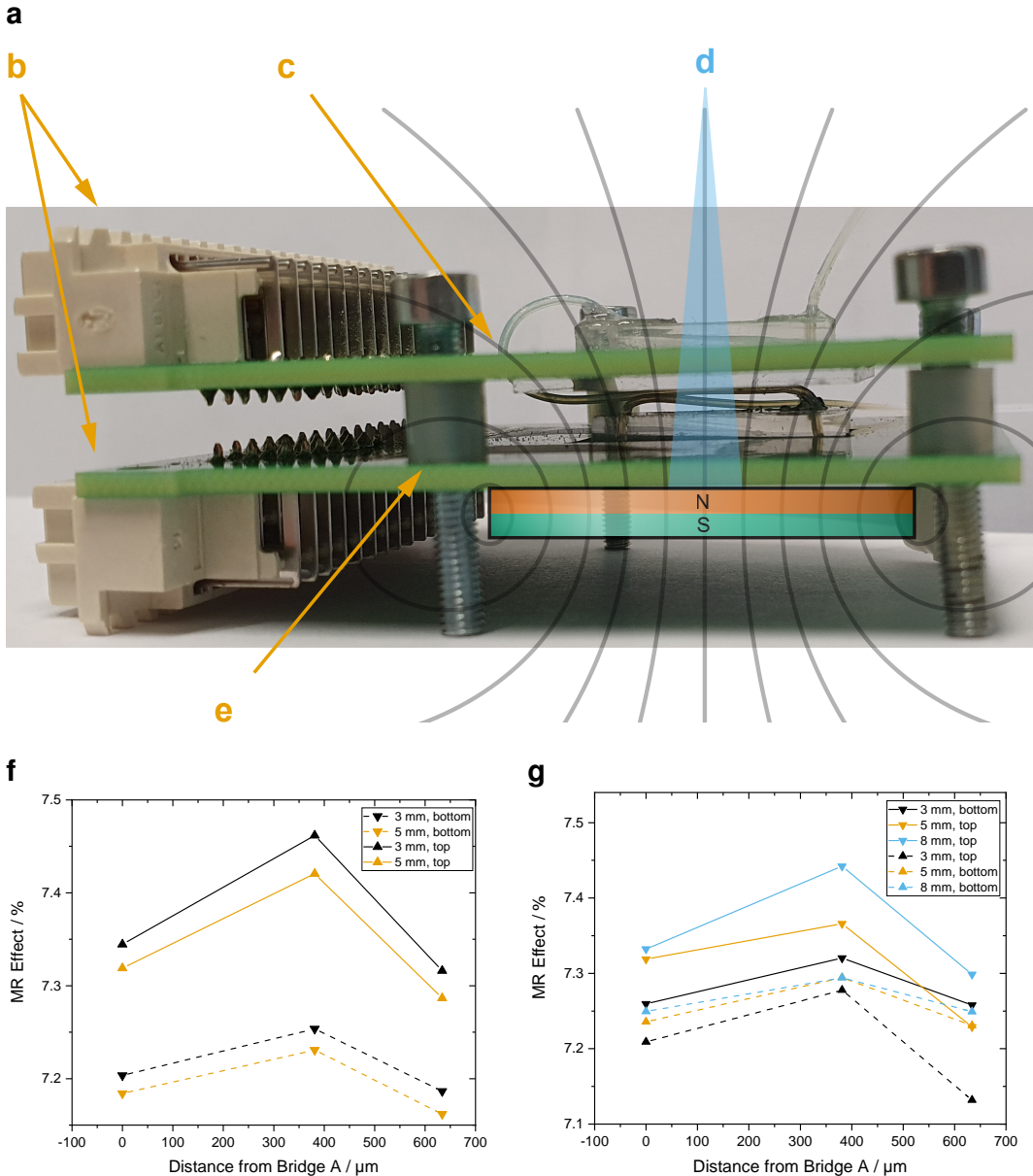


Figure 25: Hysteresis Calibration for Stacked PCB Setup

(a) Differential measurement setup: the system comprises of two separately assembled sensor PCBs (b) with nylon spacers (e) between the positional screws. (f) A hole with 3 mm diameter was drilled between the strip lines to connect the top chip outlet to the bottom chip inlet and minimize tubing length thereby. Schematically, a permanent magnet is placed below the bottom PCB. (d) The field line density respectively the area with negligibly differing field vectors is shown in the blue triangle. Because the adjustment is always carried out for a single bridge at once, this causes a systematic error.

The magneto-resistive effects of both sensors, calculated from their hystereses, are depicted for top and bottom sensors, respectively. Whereas the hysteresis was optimized for the centered sensor bridge (D or E) on the top sensor in (f), it was optimized for the bottom sensor in (g). Additionally, the height of the nylon spacers was varied from 3 mm to 8 mm but showed no statistical correlation.

Concentration Measurement in Buffer Solution

Due to the single utilized permanent magnet for two sensors, another field related issue arose during concentration measurements. This requires a step back inside the general functionality of the magnetophoretic enrichment:

Any bead flowing at an arbitrary position in the microchannel experiences a positive magnetic force by the gradient of the magnetic flux density caused by the permanent magnet which pulls perpendicular to the bottom surface. Upon coming in close proximity to the lower boundary, a gradient provoked by the lithographic nickel-iron structures starts to gain strength with the third power of the distance. This causes the beads to attach to the bottom firmly and enforces their rolling behavior. However, a fragile equilibrium between magnetophoresis and drag has to be maintained slightly in favor of Stoke's drag force for a continuous rolling motion. This ideal state is a narrow space in between two boundary cases.

First, if drag force outnumbers magnetophoresis, the beads will not migrate to the channel bottom in the top chip and hence cause a depressed concentration measurement on top. Second, if magnetophoresis outnumbers drag so that particles flow steadily in the top channel, the beads in the lower channel will stop rolling and adhere statically. In effect, the lower concentration measurement is compromised.

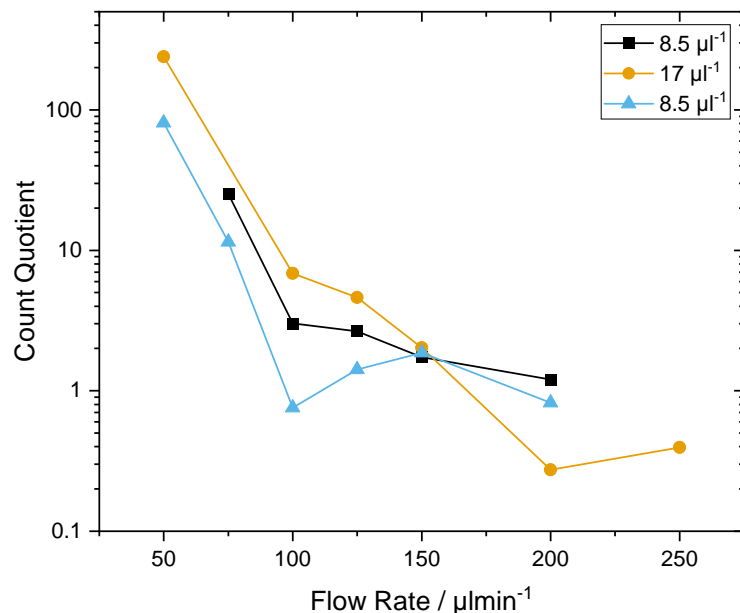


Figure 26: Optimal Differential Counting Flow Rate
Losses in different buffers and bead surfaces.

In order to find the flow rate for the optimal ratio between drag and magnetic force, measurements were performed with bead concentrations ranging from $6.5 \mu\text{L}^{-1}$ to $34 \mu\text{L}^{-1}$.⁵

⁵ The raw data is shown in Fig. 31

The quotient of both measured concentration was determined after Eq. 4.13 and plotted in Fig. 26. Although, the optimal quotient value would have been 1 theoretically, an ideal overlap was found for a flow rate of $150 \mu\text{L min}^{-1}$. However, the difficulties in assembly and operation inhibited a further usage in experiments.

2.5. Surface Modification and Biofunctionalization of the Sensor Chip Substrate

In consideration of the problems of surface instability analyzed in Sec. 2.4.1 and to avoid additional uncertainties in the experimental validation of the model from Sec. 2.2.2, a covalent functionalization of the sensor surface with neutravidin was carried out. Initially, a plate reader experiment for a qualitative statement about the shear-force stability of protein adsorption was performed. Then, different functionalization approaches with piranha and HF were tested with pure glass, PDMS, and eventually Si_3N_4 . As sophisticated chemical analyses were hardly available, the validation of these procedures was limited to indirect measurements such as tensiometry, fluorescence microscopy, and quantitative bead capture assays.

2.5.1. Physisorption

In order to quantify the adsorption stability for fluorescently-labeled, physisorbed streptavidin molecules, sensor chips were cut into 10 mm^2 pieces and glued to the bottom of a 96-well plate. Subsequently, they were equilibrated with PBS and incubated with 1 mg mL^{-1} over night. Each measurement was corrected for a blank substrate as well as the negative control with plain PBS buffer and normalized subsequently.

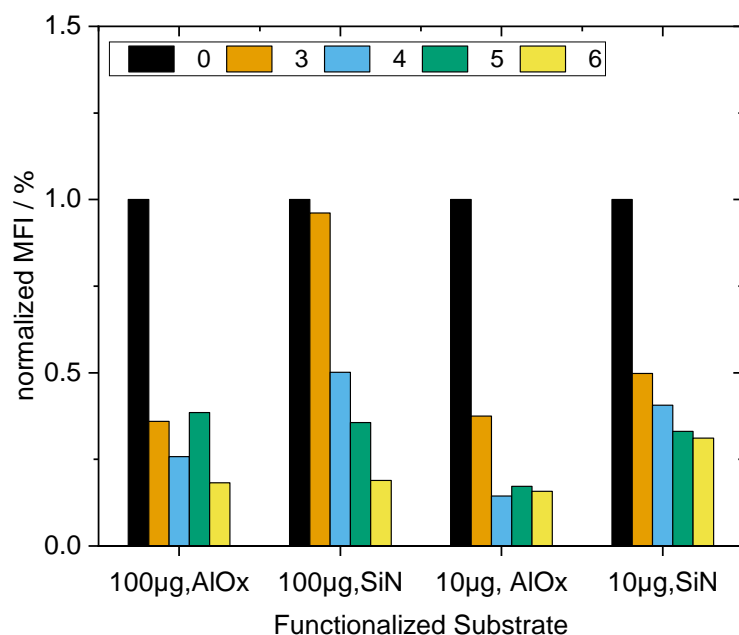


Figure 27: Surface Adsorption Stability of Neutravidin on Si_3N_4 and Aluminium oxide (Al_2O_3)

Plate reader measurement with $3 \text{ mm} \times 3 \text{ mm}$ Si_3N_4 and Al_2O_3 samples which were incubated with $100 \mu\text{g}$ and $10 \mu\text{g}$ streptavidin-atto488, respectively. The samples were subsequently washed with $200 \mu\text{L}$ PBS carefully. Fluorescence intensities were corrected with a blank substrate, the autofluorescence of PBS, and normalized eventually. Every surface reaches a mean fluorescence level of 28 % after few washing steps.

Every sample in the plate reader showed a significant surface decrease to a mean level of 28 % from the original fluorescence.(Fig. 27) Whereas proteins desorbed from both

crystals after the first washing steps equally, Si_3N_4 outperformed Al_2O_3 as more stable in steady state. (34.8 % vs. 27.5 %) However, no quantitative hypothesis could be formulated by these numbers due to the nature of their indirect measurement. Hence, the protein activity which is the crucial quantity for any bead rolling remains questionable. Nevertheless, a qualitative proposition is strongly confirmed that unspecifically adsorbed proteins are removed from any of both surfaces rapidly.

2.5.2. Evaluation of the Covalent Biofunctionalization with Optical Methods

Now, the results of several covalent surface modification procedures with various substrates are presented. Foremost, glass was used as main carrier material. On glass established protocols were then brought onto PDMS and Si_3N_4 chips. As main functionalization protocol, an activation in 7:1 piranha was carried out for 30 min. Then, the substrate was rinsed, incubated in 2 % APTES solution and in poly(acrylic) acid (PAA) subsequently after the protocol described in ???. Then a $150 \mu\text{m}$ microfluidic channel was glued to the functionalized substrate and eventually filled with 1 mg mL^{-1} of neutravidin or streptavidin-atto488, if fluorescent labeling was intended. A constant flow rate of $80 \mu\text{L min}^{-1}$ was selected for the bead capture assays under the light microscope. The general process chain is depicted in Fig. 30.

As a final result, a chemical and biological functionalization could be established to a similar degree as unspecific bonding. Measuring the count of beads per occupied area yields Fig. 28a. Again, two distinct states can be observed for biotinylated and plain beads at every modified surface.

The density of bound protein could also be varied through the incubation concentration and measured reliably both in a optical bead capture assay and the MFI of the channel in a fluorescence microscope.(Figs. 28b and 28c) The relative MFI indicates here the fraction supra the non-functionalized, PBS-filled microchannel.

However, a substantially different long-term stability could neither be measured nor compared to similar results accurately. Also, no proof for the covalent functionalization could be brought with the available methods. Nevertheless, a robust and working protocol has been developed after significant literature values which encourages the position.

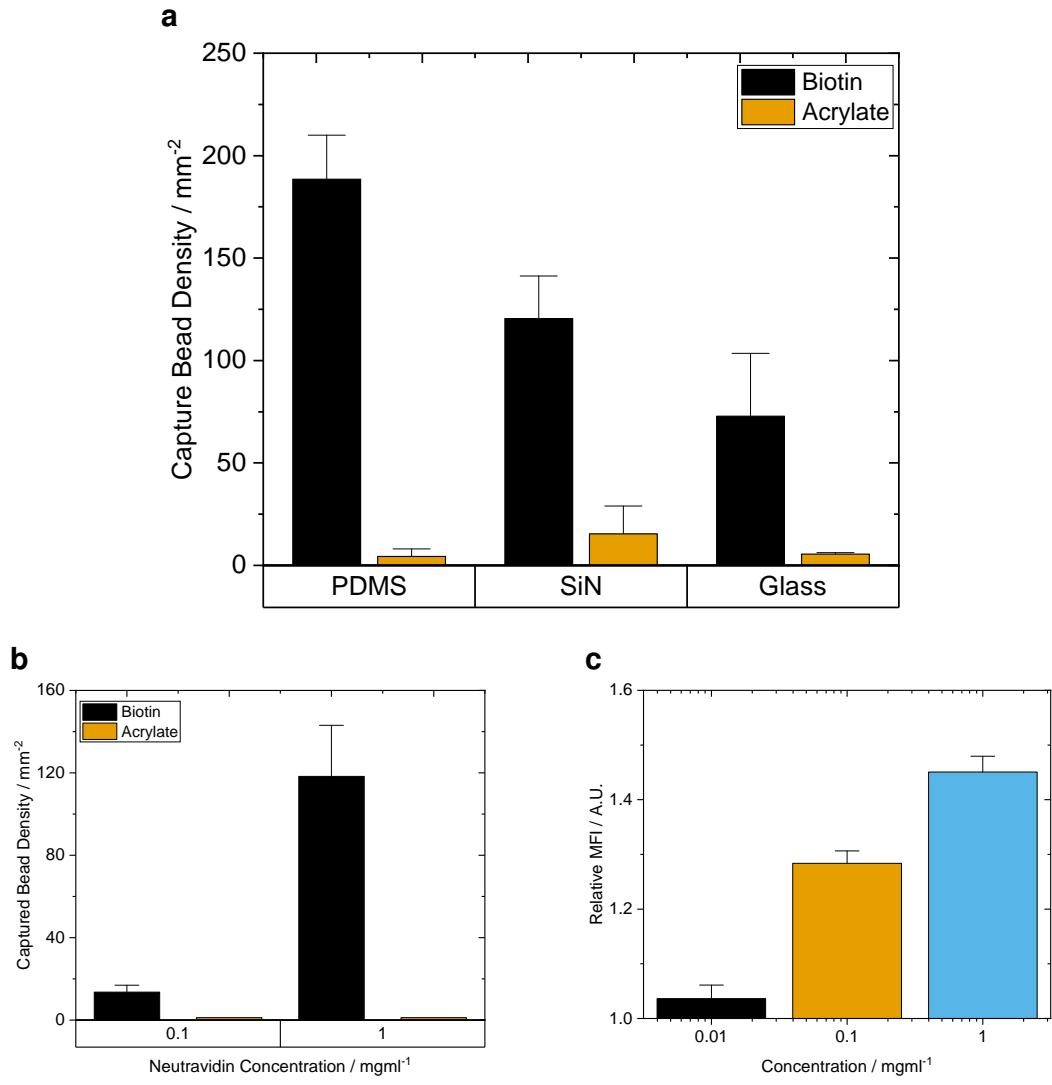


Figure 28: Optical Bead Capture Assay and Titration Fluorescence Analysis

(a) Density measurement of captured beads on the covalently functionalized surfaces of PDMS, Si_3N_4 and glass. PDMS shows the most promising density. (b) Titration of neutravidin on covalently functionalized glass with a subsequent analysis by a bead capture assay. (c) Titration of streptavidin-atto488 on covalently functionalized glass with subsequent fluorescence microscope imaging.

3. Discussion

During the course of this thesis, motions of spheroids - such as beads or cells - over the GMR-sensor have been modeled from a physics and signal processing perspective. In a magnetic field simulation it has been found that beads generate a well defined signal shape if the MNPs are distributed homogeneously over their respective surface. Thereby, the size of each MNP matters strongly. It is a strong trade-off between carrying enough magnetic momentum to get a sufficient amplitude in dipole superposition and at the same time not causing inhomogeneities in the magnetic signal. Nevertheless, a broad range from 100 nm to 1000 nm diameter of the labels showed a linear magnetization behavior above 30 % of total coverage.

In the force-equilibrium simulation, a model for a rolling motion on the bottom of a functionalized microchannel was built on basic calculus estimations. Apparently, the dominant rolling forces act on a microbead in the nN range, which leads to a necessary interaction of single to thousand proteins according to their relative bond-release force per biomolecule. This could be subject to further refinements of the MATLAB framework with the differential equations for binding kinetics [84] or the rolling motion simulation more close to the reality.

Those computational findings were adapted to 8 μm diameter microspheres which were biotinylated or antibody-coated by carbodiimide chemistry in different surface densities. On the one side, the magnetic momentum of beads could now be varied through a saturation with streptavidin-MNP conjugates and measured in the magnetic flow cytometer. On the other side, this allowed for a magnetic bead capture assay where a unspecifically functionalized channel prevented the rolling of beads with the matching ligand on their surface. Additionally, for a more robust measurement in future experiments, methods for the covalent surface modifications of glass, PDMS and Si_3N_4 have been established and analyzed by fluorescence microscopy and an optical bead capture assay.

However, the covalent nature of the surface modification - or more precisely the non-physisorption - could not be revealed during this thesis. Also the covalent functionalization procedures have never been evaluated magnetically but only optically. A comparison between both measurements bears much room for misassumptions.

Start by briefly summarizing your major findings, but without repeating exact data from the Results. This makes your novel information clear to peer reviewers and, later on, readers. It also forces you to decide which findings you should focus on in the Discussion. Thereafter, discuss possible underlying mechanisms. Why did you get these results, what is happening? Mechanisms, particularly molecular mechanisms, have very high "impact" in the natural sciences.

Next, compare your findings to those of other relevant publications and attempt to explain any discrepancies. If your findings disagree with those of others in the area, compare their publication to your own manuscript in minute detail, looking for any differences (especially in methodology) that might explain the discrepancy.

Consider the possible limitations of your own study—paradoxically, most reviewers consider an awareness and openness about potential weaknesses as a strength. However, do not forget to emphasize strengths as well.

Discuss the possible consequences of your observations and/or future investigations required or motivated. Be as concrete as possible about future perspectives. As in the abstract, writing the equivalent of “more research is needed” is meaningless—more research is always needed. Describe the hypotheses, questions or mechanisms that need to be investigated and/or methods that should be applied, concretely and concisely. And, of course, if your research findings have potential practical implications, discuss these in some detail as well.

Finally, state your conclusions—have you supported or rejected the hypothesis you posed, or obtained an answer to your research question?

Deriving Navier-Stokes equation by the Cauchy momentum equation is complex and harbors several sources of error. First, an incompressible Newtonian fluid as well as channel boundary is assumed. The used water suspensions are approximated with negligible compressibility, which is not true for the real case. Also, for blood or other shear-thinning fluids these deviations are prone for high errors.

Then, the divergence relation of the respective viscous stress (eq. 1.7) does not hold for non-uniform viscosity η .

For later studies in a matlab model, the flow velocity and shear stress computations were carried out with the error sources considered.

→ signal analysis with wavelet analysis

Third, the transient term (eq. 1.8) was neglected in all simulations, but a connected syringe pump possesses a slow rise time (Fig. 29a) and a remaining “pulsation error” in steady state (Fig. 29b). In effect, another error adds to the simulation, which is only valid after several ten seconds of the last flow rate change.

Second, the channel height varies in reality as a result of fabrication inaccuracies.

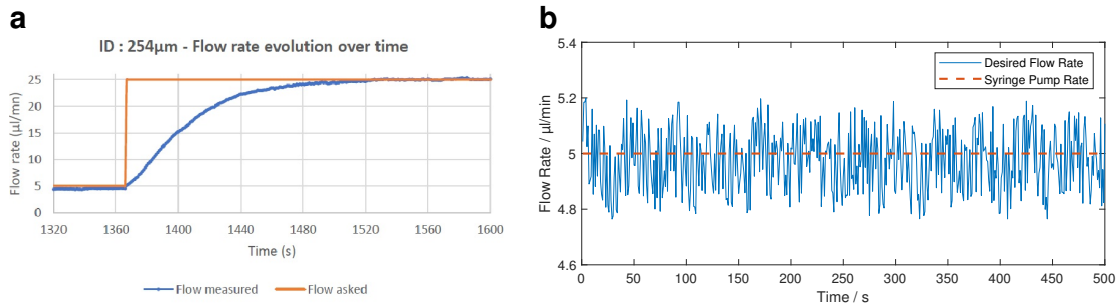


Figure 29: Syringe Pump error sources

Set flow rate: , Real Flow Rate: a Transient step answer of a syringe pump through a microtube with 254 μm inner diameter. b Steady state flow rate error around the desired $5 \mu\text{L min}^{-1}$ dispensing rate. A sinusoidal behaviour caused by the microstepping can be observed. [85]

modification of nh₂ with paa and protein like cooh

Contact angle for silanization of surface methods more useful \rightarrow should be 1st approach for characterization

Anti-Biotin-PE working? BNF-Dextran-Streptavidin unspecific binding? electrostatic surface interaction evidence covalent binding?

gas bubbles, adsprotion decrease, tubing exchange activity of protein

bead rolling with biotin-cooh, biotin-nh₂, plain-cooh, plain-nh₂ \rightarrow velocity correction factor

concentration of beads in differential setup too high, maybe better results with lower.

4. Appendix

4.1. Mathematical Notation

For simplicity, any physical unit will be abstracted here by the arbitrary function $f(\xi)$. The notation for this thesis has been defined as follows:

4.1.1. Vectorial and Scalar Units

Vector or tensor symbols are written in bold font, while normal font is used for scalar units. Forces - independently of magnitude or direction - are shown with a bold, capital \mathbf{F} . The imaginary unit is connoted as i .

Normal acting properties are multiplied with the unit outward normal (\vec{n}). The normal vector to a plane spanned by two independent vectors is calculated by the cross-product $f \times f$, while the scalar product is denoted by the centered dot $f \cdot f$.

4.1.2. Differential Operators

In the derivations, following after Eqs. 1.2 and 1.3, the gradient operator is symbolized by ∇f . The divergence operator of an arbitrary function f is utilized as $\nabla \cdot f$. The Laplace operator, in scalar context known as the second order derivative, is generalized here as $\nabla^2 f$ and equals $(\nabla \cdot \nabla) f$ respectively. It should be not confused with the capital delta Δ , which indicates the difference of a unit, such as $\Delta f = f_2 - f_1$. The identity matrix \mathbf{I} is indexed by its size, for example $\mathbf{I}_{3 \times 3}$.

$$\sum_i f(\xi = i) = \sum_{i=0}^{\infty} f(\xi = i) \quad 1.1$$

$$\int_a^b f(\xi) d\xi = F(b) - F(a) \quad 1.2$$

$$\int f(\xi) d\xi = F(\xi) + c \quad 1.3$$

4.1.3. Integration and Summation Operators

The index of an infinite sum is shown in Eq. 1.1 and starts at 0 unless specified otherwise. If the boundaries of an integral are not shown at the top and bottom (Eq. 1.2), it is considered as indefinite integral (Eq. 1.3) with the integration constant c . However, c denotes during the course of this work - due to a lack of explicitly solved integrals - concentrations. For surfaces and volumes, the integral is repeated according to the respective dimension. In the indefinite case, the unit surface is denoted by dA , and in the volumetric case by dV .

4.1.4. Equations and Inequalities

Approximated or estimated units are expressed by an equal sign with the assumption in overset or two tildes above each other. For sufficiency conditions, mostly inequalities were used. In these, double angular brackets, \ll or \gg , imply an value difference of at least one order of magnitude. Postulated conditions are indicated by an exclamation mark above the equal sign: $\stackrel{!}{=}$.

4.2. Additional Figures

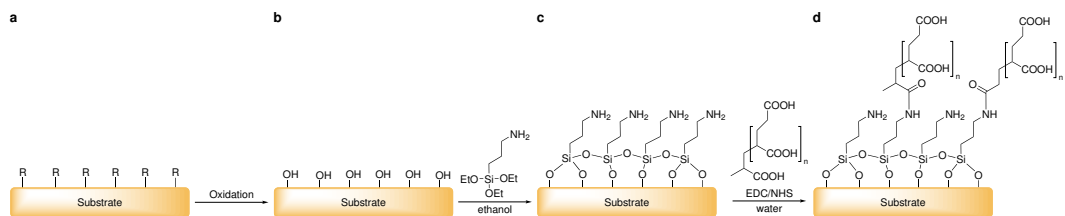


Figure 30: General process chain of chemical surface modification

Any substrate with various surface groups R (a) is oxidized to exhibit hydroxyl groups.(b). Then a silane SAM is attached (c) and subsequently modified by carbodiimide chemistry with PAA. (d)

größer, schöner

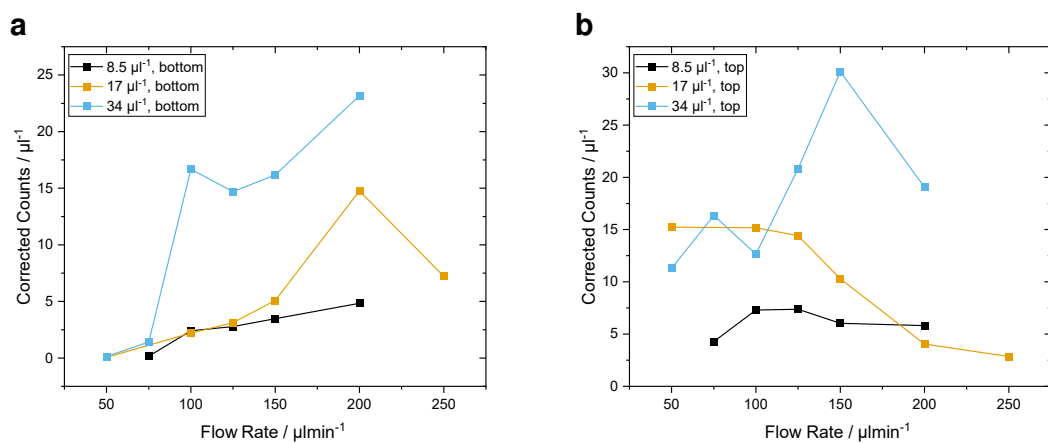


Figure 31: Flow Rate Dependency of Differential Counting Setup

(a) Optimized for top sensor (b) Optimized for bottom sensor

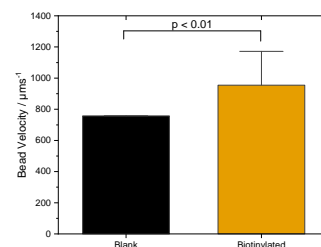


Figure 32: Measured Bead Velocity

Not sure what to say about velocity itself. Maybe remove completely, p < 0.01

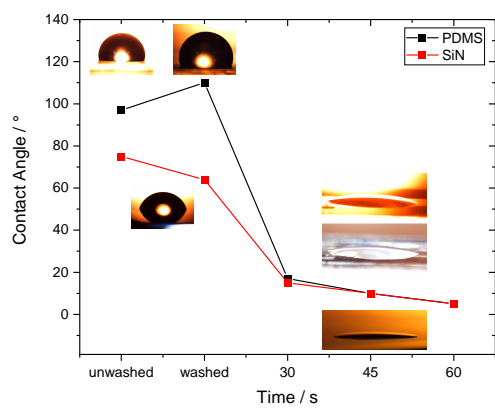


Figure 33: Hydrophobicity Analysis of PDMS under Plasma Exposure

For an optimal plasma bond to glass, Si_3N_4 and PDMS, the contact angle was measured after treatment. The initial decrease until 45 s declares the optimum around this time. Longer times should be avoided consequently to prohibit further surface damages by reactive ions.